

1 **High-level cognition during story listening is reflected in
2 high-order dynamic correlations in neural activity patterns**

3 Lucy L. W. Owen¹, Thomas H. Chang^{1,2}, and Jeremy R. Manning^{1,†}

¹Department of Psychological and Brain Sciences,
Dartmouth College, Hanover, NH

²Amazon.com, Seattle, WA

†Address correspondence to jeremy.r.manning@dartmouth.edu

4 August 12, 2021

5 **Abstract**

6 Our thoughts arise from coordinated patterns of interactions between brain structures that change
7 with our ongoing experiences. High-order dynamic correlations in neural activity patterns reflect different
8 subgraphs of the brain's functional connectome that display homologous lower-level dynamic correlations.
9 Here we test the hypothesis that high-level cognition is reflected in high-order dynamic correlations in brain
10 activity patterns. We develop an approach to estimating high-order dynamic correlations in timeseries data,
11 and we apply the approach to neuroimaging data collected as human participants either listen to a ten-
12 minute story or listen to a temporally scrambled version of the story. We train across-participant pattern
13 classifiers to decode (in held-out data) when in the session each neural activity snapshot was collected. We
14 find that classifiers trained to decode from high-order dynamic correlations yield the best performance on
15 data collected as participants listened to the (unscrambled) story. By contrast, classifiers trained to decode
16 data from scrambled versions of the story yielded the best performance when they were trained using first-
17 order dynamic correlations or non-correlational activity patterns. We suggest that as our thoughts become
18 more complex, they are reflected in higher-order patterns of dynamic network interactions throughout the
19 brain.

20 **Introduction**

21 A central goal in cognitive neuroscience is to elucidate the neural code: i.e., the mapping between (a) mental
22 states or cognitive representations and (b) neural activity patterns. One means of testing models of the
23 neural code is to ask how accurately that model is able to "translate" neural activity patterns into known
24 (or hypothesized) mental states or cognitive representations^{1–9}. Training decoding models on different
25 types of neural features (Fig. 1a) can also help to elucidate which specific aspects of neural activity patterns
26 are informative about cognition and, by extension, which types of neural activity patterns might compose
27 the neural code. For example, prior work has used region of interest analyses to estimate the anatomical
28 locations of specific neural representations¹⁰, or to compare the relative contributions to the neural code
29 of multivariate activity patterns versus dynamic correlations between neural activity patterns^{11,12}. An

30 emerging theme in this literature is that cognition is mediated by dynamic interactions between brain
31 structures^{13–25}.

32 [Figure 1 about here.]

33 Studies of the neural code to date have primarily focused on univariate or multivariate neural patterns²,
34 or (more recently) on patterns of dynamic first-order correlations (i.e., interactions between pairs of brain
35 structures^{11,12,18,20–22}). What might the future of this line of work hold? For example, is the neural code
36 implemented through higher-order interactions between brain structures²⁶? Second-order correlations re-
37 flect homologous patterns of correlation. In other words, if the dynamic patterns of correlations between
38 two regions, *A* and *B*, are similar to those between two other regions, *C* and *D*, this would be reflected
39 in the second-order correlations between (*A*–*B*) and (*C*–*D*). In this way, second-order correlations identify
40 similarities and differences between subgraphs of the brain’s connectome. Analogously, third-order cor-
41 relations reflect homologies between second-order correlations—i.e., homologous patterns of homologous
42 interactions between brain regions. More generally, higher-order correlations reflect homologies between
43 patterns of lower-order correlations. We can then ask: which “orders” of interaction are most reflective of
44 high-level cognitive processes?

45 One reason one might expect to see homologous networks in a dataset is related to the notion that
46 network dynamics reflect ongoing neural computations or cognitive processing²⁷. If the nodes in two brain
47 networks are interacting (within each network) in similar ways then, according to our characterization
48 of network dynamics, we refer to the similarities between those patterns of interaction as higher-order
49 correlations. When higher-order correlations are themselves changing over time, we can also attempt to
50 capture and characterize those high-order dynamics.

51 Another central question pertains to the extent to which the neural code is carried by activity patterns
52 that directly reflect ongoing cognition^{1,2}, versus the dynamic properties of the network structure itself,
53 independent of specific activity patterns in any given set of regions¹⁶. For example, graph measures
54 such as centrality and degree²⁸ may be used to estimate how a given brain structure is “communicating”
55 with other structures, independently of the specific neural representations carried by those structures.
56 If one considers a brain region’s position in the network (e.g., its eigenvector centrality) as a dynamic
57 property, one can compare how the positions of different regions are correlated, and/or how those patterns
58 of correlations change over time. We can also compute higher-order patterns in these correlations to
59 characterize homologous subgraphs in the connectome that display similar changes in their constituent
60 brain structures’ interactions with the rest of the brain.

61 To gain insights into the above aspects of the neural code, we developed a computational framework

for estimating dynamic high-order correlations in timeseries data. This framework provides an important advance, in that it enables us to examine patterns of higher-order correlations that are computationally intractable to estimate via conventional methods. Given a multivariate timeseries, our framework provides timepoint-by-timepoint estimates of the first-order correlations, second-order correlations, and so on. Our approach combines a kernel-based method for computing dynamic correlations in timeseries data with a dimensionality reduction step (Fig. 1b) that projects the resulting dynamic correlations into a low-dimensional space. We explored two dimensionality reduction approaches: principle components analysis²⁹ (PCA), which preserves an approximately invertible transformation back to the original data³⁰⁻³², and a second non-invertible algorithm for computing dynamic patterns in eigenvector centrality³³. This latter approach characterizes correlations between each feature dimension's relative position in the network (at each moment in time) in favor of the specific activity histories of different features^{26,34,35}.

We validated our approach using synthetic data where the underlying correlations were known. We then applied our framework to a neuroimaging dataset collected as participants listened to either an audio recording of a ten-minute story, listened to a temporally scrambled version of the story, or underwent a resting state scan³⁶. Temporal scrambling has been used in a growing number of studies, largely by Uri Hasson's group, to identify brain regions that are sensitive to higher-order and longer-timescale information (e.g., cross-sensory integration, rich narrative meaning, complex situations, etc.) versus regions that are primarily sensitive to low-order (e.g., sensory) information. For example,³⁷ argues that when brain areas are sensitive to fine versus coarse temporal scrambling, this indicates that they are "higher order" in the sense that they process contextual information pertaining to further-away timepoints. By contrast, low-level regions, such as primary sensory cortices, do not meaningfully change their responses (after correcting for presentation order) even when the stimulus is scrambled at fine timescales.

We used a subset of the story listening and rest data to train across-participant classifiers to decode listening times (of groups of participants) using a blend of neural features (comprising neural activity patterns, as well as different orders of dynamic correlations between those patterns that were inferred using our computational framework). We found that both the PCA-based and eigenvector centrality-based approaches yielded neural patterns that could be used to decode accurately (i.e., well above chance). Both approaches also yielded the best decoding accuracy for data collected during (intact) story listening when high-order (PCA: second-order; eigenvector centrality: fourth-order) dynamic correlation patterns were included as features. When we trained classifiers on the scrambled stories or resting state data, only (relatively) lower-order dynamic patterns were informative to the decoders. Taken together, our results indicate that high-level cognition is supported by high-order dynamic patterns of communication between brain structures.

95 **Results**

96 We sought to understand whether high-level cognition is reflected in dynamic patterns of high-order correla-
97 tions. To that end, we developed a computational framework for estimating the dynamics of stimulus-driven
98 high-order correlations in multivariate timeseries data (see Dynamic inter-subject functional connectivity
99 (DISFC) and Dynamic higher-order correlations). We evaluated the efficacy of this framework at recovering
100 known patterns in several synthetic datasets (see Synthetic data: simulating dynamic first-order corre-
101 lations and Synthetic data: simulating dynamic higher-order correlations). We then applied the framework
102 to a public fMRI dataset collected as participants listened to an auditorily presented story, listened to a
103 temporally scrambled version of the story, or underwent a resting state scan (see Functional neuroimaging
104 data collected during story listening). We used the relative decoding accuracies of classifiers trained on
105 different sets of neural features to estimate which types of features reflected ongoing cognitive processing.

106 **Recovering known dynamic first-order correlations**

107 We generated synthetic datasets that differed in how the underlying first-order correlations changed over
108 time. For each dataset, we applied Equation 4 with a variety of kernel shapes and widths. We assessed how
109 well the true underlying correlations at each timepoint matched the recovered correlations (Fig. 2). For every
110 kernel and dataset we tested, our approach recovered the correlation dynamics we embedded into the data.
111 However, the quality of these recoveries varied across different synthetic datasets in a kernel-dependent
112 way.

113 [Figure 2 about here.]

114 In general, wide monotonic kernel shapes (Laplace, Gaussian), and wider kernels (within a shape),
115 performed best when the correlations varied gradually from moment-to-moment (Figs. 2a, c, and d). In the
116 extreme, as the rate of change in correlations approaches 0 (Fig. 2a), an infinitely wide kernel would exactly
117 recover the Pearson's correlation (e.g., compare Eqns. 1 and 4).

118 When the correlation dynamics were unstructured in time (Fig. 2b), a Dirac δ kernel (infinitely narrow)
119 performed best. This is because, when every timepoint's correlations are independent of the correlations at
120 every other timepoint, averaging data over time dilutes the available signal. Following a similar pattern,
121 holding kernel shape fixed, narrower kernel parameters better recovered randomly varying correlations.

122 **Recovering known dynamic higher-order correlations**

123 Following our approach to evaluating our ability to recover known dynamic first-order correlations from
124 synthetic data, we generated an analogous second set of synthetic datasets that we designed to exhibit
125 known dynamic first-order and second-order correlations (see Synthetic data: simulating dynamic higher-
126 order correlations). We generated a total of 400 datasets (100 datasets for each category) that varied in how
127 the first-order and second-order correlations changed over time. We then repeatedly applied Equation 4
128 using the overall best-performing kernel from our first-order tests (a Laplace kernel with a width of 20;
129 Fig. 2) to assess how closely the recovered dynamic correlations matched the dynamic correlations we had
130 embedded into the datasets.

131 Overall, we found that we could reliably recover both first-order and second-order correlations from the
132 synthetic data (Fig. 3). When the correlations were stable for longer intervals, or changed gradually (constant,
133 ramping, and event datasets), recovery performance was relatively high, and we were better able to recover
134 dynamic first-order correlations than second-order correlations. This is because errors in our estimation
135 procedure at lower orders necessarily propagate to higher orders (since lower-order correlations are used to
136 estimate higher-order correlations). Conversely, when the correlations were particularly unstable (random
137 datasets), we better recovered second-order correlations. This is because noise in our data generation
138 procedure propagates from higher orders to lower orders (see Synthetic data: simulating dynamic high-
139 order correlations).

140 [Figure 3 about here.]

141 We also examined the impact of the data duration (Fig. S3) and complexity (number of zero-order features;
142 Fig. S4) on our ability to accurately recover ground truth first-order and second-order dynamic correlations.
143 In general, we found that our approach better recovers ground truth dynamic correlations from longer
144 duration timeseries data. We also found that our approach tends to best recover data generated using fewer
145 zero-order features (i.e., lower complexity), although this tendency was not strictly monotonic. Further,
146 because our data generation procedure requires $O(K^4)$ memory to generate a second-order timeseries with K
147 zero-order features, we were not able to fully explore how the number of zero-order features affects recovery
148 accuracy as the number of features gets larger (e.g., as it approaches the number of features present in the
149 fMRI data we examine below). Although we were not able to formally test this to our satisfaction, we expect
150 that accurately estimating dynamic high-order correlations would require data with many more zero-order
151 features than we were able to simulate. Our reasoning is that high-order correlations necessarily involve
152 larger numbers of lower-order features, so achieving adequate “resolution” high-order timeseries might
153 require many low-order features.

154 Taken together, our explorations using synthetic data indicated that we are able to partially, but not
155 perfectly, recover ground truth dynamic first-order and second-order correlations. This suggests that our
156 modeling approach provides a meaningful (if noisy) estimate of high-order correlations. We next turned
157 to analyses of human fMRI data to examine whether the recovered dynamics might reflect the dynamics of
158 human cognition during a naturalistic story-listening task.

159 **Cognitively relevant dynamic high-order correlations in fMRI data**

160 We used across-participant temporal decoders to identify cognitively relevant neural patterns in fMRI data
161 (see Forward inference and decoding accuracy). The dataset we examined³⁶ comprised four experimental
162 conditions that exposed participants to stimuli that varied systematically in how cognitively engaging they
163 were. The intact experimental condition (intact) had participants listen to an audio recording of a 10-minute
164 story. The paragraph-scrambled experimental condition (paragraph) had participants listen to a temporally
165 scrambled version of the story, where the paragraphs occurred out of order (but where the same total set of
166 paragraphs were presented over the full listening interval). All participants in this condition experienced
167 the scrambled paragraphs in the same order. The word-scrambled experimental condition (word) had
168 participants listen to a temporally scrambled version of the story where the words in the story occurred
169 in a random order. All participants in the word condition experienced the scrambled words in the same
170 order. Finally, in a rest experimental condition (rest), participants lay in the scanner with no overt stimulus,
171 with their eyes open (blinking as needed). This public dataset provided a convenient means of testing our
172 hypothesis that different levels of cognitive processing and engagement are reflected in different orders of
173 brain activity dynamics.

174 [Figure 4 about here.]

175 In brief, we computed timeseries of dynamic high-order correlations that were similar across participants
176 in each of two randomly assigned groups: a training group and a test group. We then trained classifiers
177 on the training group's data to match each sample from the test group with a stimulus timepoint. Each
178 classifier comprised a weighted blend of neural patterns that reflected up to n^{th} -order dynamic correlations
179 (see Feature weighting and testing). We repeated this process for $n \in \{0, 1, 2, \dots, 10\}$. Our examinations of
180 synthetic data suggested that none of the kernels we examined were “universal” in the sense of optimally
181 recovering underlying correlations regardless of the temporal structure of those correlations. We found a
182 similar pattern in the (real) fMRI data, whereby different kernels yielded different decoding accuracies, but
183 no single kernel emerged as the clear “best.” In our analyses of neural data, we therefore averaged our

184 decoding results over a variety of kernel shapes and widths in order to identify results that were robust to
185 specific kernel parameters (see Identifying robust decoding results).

186 Our approach to estimating dynamic high-order correlations entails mapping the high-dimensional
187 feature space of correlations (represented by a T by $O(K^2)$ matrix) onto a lower-dimensional feature space
188 (represented by a T by K matrix). We carried out two sets of analyses that differed in how this mapping was
189 computed. The first set of analyses used PCA to find a low-dimensional embedding of the original dynamic
190 correlation matrices (Fig. 4a,b). The second set of analyses characterized correlations in dynamics of each
191 feature's eigenvector centrality, but did not preserve the underlying activity dynamics (Fig. 4c,d).

192 [Figure 5 about here.]

193 Both sets of temporal decoding analyses yielded qualitatively similar results for the auditory (non-rest)
194 conditions of the experiment (Fig. 4: pink, green, and teal lines; Fig. 5: three leftmost columns). The highest
195 decoding accuracy for participants who listened to the intact (unscrambled) story was achieved using high-
196 order dynamic correlations (PCA: second-order; eigenvector-centrality: fourth-order). Scrambled versions
197 of the story were best decoded by lower-order correlations (PCA/paragraph: first-order; PCA/word: order
198 zero; eigenvector centrality/paragraph: order zero; eigenvector centrality/word: order zero). The two sets
199 of analyses yielded different decoding results on resting state data (Fig. 4: purple lines; Fig. 5: rightmost
200 column). We note that, while the resting state times could be decoded reliably, the accuracies were only very
201 slightly above chance. We speculate that the decoders might have picked up on attentional drift, boredom,
202 or tiredness; we hypothesize that these all increased throughout the resting state scan. The decoders might
203 be picking up on aspects of these loosely defined cognitive states that are common across individuals. The
204 PCA-based approach achieved the highest resting state decoding accuracy using order zero features (non-
205 correlational, activation-based), whereas the eigenvector centrality-based approach achieved the highest
206 resting state decoding accuracy using second-order correlations. Taken together, these analyses indicate
207 that high-level cognitive processing (while listening to the intact story) is reflected in the dynamics of high-
208 order correlations in brain activity, whereas lower-level cognitive processing (while listening to scrambled
209 versions of the story that lack rich meaning) is reflected in the dynamics of lower-order correlations and
210 non-correlational activity dynamics. Further, these patterns are associated both with the underlying activity
211 patterns (characterized using PCA) and also with the changing relative positions that different brain areas
212 occupy in their associated networks (characterized using eigenvector centrality).

213 [Figure 6 about here.]

214 Having established that patterns of high-order correlations are informative to decoders, we next won-
215 dered which specific networks of brain regions contributed most to these patterns. As a representative

example, we selected the kernel parameters that yielded decoding accuracies that were the most strongly correlated (across conditions and orders) with the average accuracies across all of the kernel parameters we examined. Using Figure 4c as a template, the best-matching kernel was a Laplace kernel with a width of 50 (see Kernel-based approach for computing dynamic correlations and Fig. S9). We used this kernel to compute a single K by K n^{th} -order DISFC matrix for each experimental condition. We then used Neurosynth³⁸ to compute the terms most highly associated with the most strongly correlated pairs of regions in each of these matrices (Fig. 6; see Reverse inference).

For all of the story listening conditions (intact, paragraph, and word; top three rows of Fig. 6), we found that first- and second-order correlations were most strongly associated with auditory and speech processing areas. During intact story listening, third-order correlations reflected integration with visual areas, and fourth-order correlations reflected integration with areas associated with high-level cognition and cognitive control, such as the ventrolateral prefrontal cortex. However, when participants listened to temporally scrambled stories, these higher-order correlations instead involved interactions with additional regions associated with speech and semantic processing (second and third rows of Fig. 6). By contrast, we found a much different set of patterns in the resting state data (Fig. 6, bottom row). First-order resting state correlations were most strongly associated with regions involved in counting and numerical understanding. Second-order resting state correlations were strongest in visual areas; third-order correlations were strongest in task-positive areas; and fourth-order correlations were strongest in regions associated with autobiographical and episodic memory. We carried out analogous analyses to create maps (and decode the top associated Neurosynth terms) for up to fifteenth-order correlations (Figs. S5, S6, S7, and S8). Of note, examining fifteenth-order correlations between 700 nodes using conventional methods would have required storing roughly $\frac{700^{2 \times 15}}{2} \approx 1.13 \times 10^{85}$ floating point numbers—assuming single-precision (32 bits each), this would require roughly 32 times as many bits as there are molecules in the known universe! Although these fifteenth-order correlations do appear (visually) to have some well-formed structure, we provide this latter example primarily as a demonstration of the efficiency and scalability of our approach.

Discussion

We tested the hypothesis that high-level cognition is reflected in high-order brain network dynamics^{19,26}. We examined high-order network dynamics in functional neuroimaging data collected during a story listening experiment. When participants listened to an auditory recording of the story, participants exhibited similar high-order brain network dynamics. By contrast, when participants instead listened to temporally scrambled recordings of the story, only lower-order brain network dynamics were similar across participants.

247 Our results indicate that higher orders of network interactions support higher-level aspects of cognitive
248 processing (Fig. 7).

249 [Figure 7 about here.]

250 The notion that cognition is reflected in (and possibly mediated by) patterns of first-order network dy-
251 namics has been suggested by or proposed in myriad empirical studies and reviews^{11,12,17,18,20–22,24,25,32,39–42}.
252 Our study extends this line of work by finding cognitively relevant higher-order network dynamics that
253 reflect ongoing cognition. Our findings also complement other work that uses graph theory and topology
254 to characterize how brain networks reconfigure during cognition^{16,26,30,31,34,35,43}.

255 An open question not addressed by our study pertains to how different structures integrate incoming
256 information with different time constants. For example, one line of work suggests that the cortical surface
257 comprises a structured map such that nearby brain structures process incoming information at similar
258 timescales. Low-level sensory areas integrate information relatively quickly, whereas higher-level regions
259 integrate information relatively slowly^{37,44–49}. A similar hierarchy appears to play a role in predicting future
260 events⁵⁰. Other related work in human and mouse brains indicates that the temporal response profile of a
261 given brain structure may relate to how strongly connected that structure is with other brain areas⁵¹. Further
262 study is needed to understand the role of temporal integration at different scales of network interaction,
263 and across different anatomical structures. Importantly, our analyses do not speak to the physiological
264 basis of higher-order dynamics, and could reflect nonlinearities, chaotic patterns, non-stationarities, and/or
265 multistability, etc. However, our decoding analyses do indicate that higher-order dynamics are consistent
266 across individuals, and therefore unlikely to reflect non-stimulus-driven dynamics that are unlikely to be
267 similar across individuals.

268 One limitation of our approach relates to how noise propagates in our estimation procedure. Specifi-
269 cally, our procedure for estimating high-order dynamic correlations depends on estimates of lower-order
270 dynamic correlations. This means that our measures of which higher-order patterns are reliable and stable
271 across experimental conditions are partially confounded with the stability of lower-order patterns. Prior
272 work suggests that the stability of what we refer to here as first-order dynamics likely varies across the
273 experimental conditions we examined³⁶. Therefore a caveat to our claim that richer stimuli evoke more
274 stable higher-order dynamics is that our approach assumes that those high-order dynamics reflect relations
275 or interactions between lower-order features.

276 Another potential limitation of our approach relates to recent work suggesting that the brain undergoes
277 rapid state changes, for example across event boundaries^{44, 52} used hidden semi-Markov models to estimate
278 state-specific network dynamics⁵³. Our general approach might be extended by considering putative state

279 transitions. For example, rather than weighting all timepoints using a similar kernel (Eqn. 4), the kernel
280 function could adapt on a timepoint-by-timepoint basis such that only timepoints determined to be in the
281 same “state” were given non-zero weight.

282 Identifying high-order network dynamics associated with high-level cognition required several im-
283 portant methods advances. First, we used kernel-based dynamic correlations to extended the notion of
284 (static) inter-subject functional connectivity³⁶ to a dynamic measure of inter-subject functional connectivity
285 (DISFC) that does not rely on sliding windows¹¹, and that may be computed at individual timepoints. This
286 allowed us to precisely characterize stimulus-evoked network dynamics that were similar across individ-
287 uals. Second, we developed a computational framework for efficiently and scalably estimating high-order
288 dynamic correlations. Our approach uses dimensionality reduction algorithms and graph measures to
289 obtain low-dimensional embeddings of patterns of network dynamics. Third, we developed an analysis
290 framework for identifying robust decoding results by carrying out our analyses using a range of parameter
291 values and identifying which results were robust to specific parameter choices. By showing that high-level
292 cognition is reflected in high-order network dynamics, we have elucidated the next step on the path towards
293 understanding the neural basis of cognition.

294 Methods

295 Our general approach to efficiently estimating high-order dynamic correlations comprises four general
296 steps (Fig. 8). First, we derive a kernel-based approach to computing dynamic pairwise correlations in
297 a T (timepoints) by K (features) multivariate timeseries, \mathbf{X}_0 . This yields a T by $O(K^2)$ matrix of dynamic
298 correlations, \mathbf{Y}_1 , where each row comprises the upper triangle and diagonal of the correlation matrix at
299 a single timepoint, reshaped into a row vector (this reshaped vector is $(\frac{K^2-K}{2} + K)$ -dimensional). Second,
300 we apply a dimensionality reduction step to project the matrix of dynamic correlations back onto a K -
301 dimensional space. This yields a T by K matrix, \mathbf{X}_1 , that reflects an approximation of the dynamic correlations
302 reflected in the original data. Third, we use repeated applications of the kernel-based dynamic correlation
303 step to \mathbf{X}_n and the dimensionality reduction step to the resulting \mathbf{Y}_{n+1} to estimate high-order dynamic
304 correlations. Each application of these steps to a T by K time series \mathbf{X}_n yields a T by K matrix, \mathbf{X}_{n+1} , that
305 reflects the dynamic correlations between the columns of \mathbf{X}_n . In this way, we refer to n as the order of the
306 timeseries, where \mathbf{X}_0 (order 0) denotes the original data and \mathbf{X}_n denotes (approximated) n^{th} -order dynamic
307 correlations between the columns of \mathbf{X}_0 . Finally, we use a cross-validation-based decoding approach to
308 evaluate how well information contained in a given order (or weighted mixture of orders) may be used
309 to decode relevant cognitive states. If including a given \mathbf{X}_n in the feature set yields higher classification

accuracy on held-out data, we interpret this as evidence that the given cognitive states are reflected in patterns of n^{th} -order correlations.

All of the code used to produce the figures and results in this manuscript, along with links to the corresponding datasets, may be found at github.com/ContextLab/timecorr-paper. In addition, we have released a Python toolbox for computing dynamic high-order correlations in timeseries data; our toolbox may be found at timecorr.readthedocs.io.

[Figure 8 about here.]

Kernel-based approach for computing dynamic correlations

Given a T by K matrix of observations, \mathbf{X} , we can compute the (static) Pearson's correlation between any pair of columns, $\mathbf{X}(\cdot, i)$ and $\mathbf{X}(\cdot, j)$ using²⁹:

$$\text{corr}(\mathbf{X}(\cdot, i), \mathbf{X}(\cdot, j)) = \frac{\sum_{t=1}^T (\mathbf{X}(t, i) - \bar{\mathbf{X}}(\cdot, i))(\mathbf{X}(t, j) - \bar{\mathbf{X}}(\cdot, j))}{\sqrt{\sum_{t=1}^T \sigma_{\mathbf{X}(\cdot, i)}^2 \sigma_{\mathbf{X}(\cdot, j)}^2}}, \text{ where} \quad (1)$$

$$\bar{\mathbf{X}}(\cdot, k) = \frac{1}{T} \sum_{t=1}^T \mathbf{X}(t, k), \text{ and} \quad (2)$$

$$\sigma_{\mathbf{X}(\cdot, k)}^2 = \frac{1}{T} \sum_{t=1}^T (\mathbf{X}(t, k) - \bar{\mathbf{X}}(\cdot, k))^2 \quad (3)$$

We can generalize this formula to compute time-varying correlations by incorporating a kernel function that takes a time t as input, and returns how much the observed data at each timepoint $\tau \in [-\infty, \infty]$ contributes to the estimated instantaneous correlation⁵⁴ at time t (Fig. 9).

[Figure 9 about here.]

Given a kernel function $\kappa_t(\cdot)$ for timepoint t , evaluated at timepoints $\tau \in [1, \dots, T]$, we can update the static correlation formula in Equation 1 to estimate the instantaneous correlation at timepoint t :

$$\text{timecorr}_{\kappa_t}(\mathbf{X}(\cdot, i), \mathbf{X}(\cdot, j)) = \frac{\sum_{\tau=1}^T (\mathbf{X}(\tau, i) - \widetilde{\mathbf{X}}_{\kappa_t}(\cdot, i))(\mathbf{X}(\tau, j) - \widetilde{\mathbf{X}}_{\kappa_t}(\cdot, j))}{\sqrt{\sum_{\tau=1}^T \widetilde{\sigma}_{\kappa_t}^2(\mathbf{X}(\cdot, i)) \widetilde{\sigma}_{\kappa_t}^2(\mathbf{X}(\cdot, j))}}, \text{ where} \quad (4)$$

$$\widetilde{\mathbf{X}}_{\kappa_t}(\cdot, k) = \sum_{\tau=1}^T \kappa_t(\tau) \mathbf{X}(\tau, k), \quad (5)$$

$$\widetilde{\sigma}_{\kappa_t}^2(\mathbf{X}(\cdot, k)) = \sum_{\tau=1}^T (\mathbf{X}(\tau, k) - \widetilde{\mathbf{X}}_{\kappa_t}(\cdot, k))^2. \quad (6)$$

Here $\text{timecorr}_{\kappa_t}(\mathbf{X}(\cdot, i), \mathbf{X}(\cdot, j))$ reflects the correlation at time t between columns i and j of \mathbf{X} , estimated using

323 the kernel κ_t . We evaluate Equation 4 in turn for each pair of columns in \mathbf{X} and for kernels centered on each
 324 timepoint in the timeseries, respectively, to obtain a T by K by K timeseries of dynamic correlations, \mathbf{Y} . For
 325 convenience, we then reshape the upper triangles and diagonals of each timepoint's symmetric correlation
 326 matrix into a row vector to obtain an equivalent T by $(\frac{K^2-K}{2} + K)$ matrix.

327 **Dynamic inter-subject functional connectivity (DISFC)**

Equation 4 provides a means of taking a single observation matrix, \mathbf{X}_n and estimating the dynamic correlations from moment to moment, \mathbf{Y}_{n+1} . Suppose that one has access to a set of multiple observation matrices that reflect the same phenomenon. For example, one might collect neuroimaging data from several experimental participants, as each participant performs the same task (or sequence of tasks). Let $\mathbf{X}_n^1, \mathbf{X}_n^2, \dots, \mathbf{X}_n^P$ reflect the T by K observation matrices ($n = 0$) or reduced correlation matrices ($n > 0$) for each of P participants in an experiment. We can use inter-subject functional connectivity^{36,55} (ISFC) to compute the stimulus-driven correlations reflected in the multi-participant dataset at a given timepoint t using:

$$\bar{\mathbf{C}}(t) = M \left(R \left(\frac{1}{2P} \sum_{p=1}^P Z(\mathbf{Y}_{n+1}^p(t))^\top + Z(\mathbf{Y}_{n+1}^p(t)) \right) \right), \quad (7)$$

where M extracts and vectorizes the upper triangle and diagonal of a symmetric matrix, Z is the Fisher z -transformation⁵⁶:

$$Z(r) = \frac{\log(1+r) - \log(1-r)}{2}, \quad (8)$$

R is the inverse of Z :

$$R(z) = \frac{\exp(2z-1)}{\exp(2z+1)}, \quad (9)$$

and $\mathbf{Y}_{n+1}^p(t)$ denotes the correlation matrix at timepoint t (Eqn. 4) between each column of \mathbf{X}_n^p and each column of the average \mathbf{X}_n from all other participants, $\bar{\mathbf{X}}_n^{\setminus p}$:

$$\bar{\mathbf{X}}_n^{\setminus p} = \frac{1}{P-1} \sum_{q \in \setminus p} \mathbf{X}_n^q, \quad (10)$$

328 where $\setminus p$ denotes the set of all participants other than participant p . In this way, the T by $(\frac{K^2-K}{2} + K)$ DISFC
 329 matrix $\bar{\mathbf{C}}$ provides a time-varying extension of the ISFC approach developed by³⁶.

330 **Low-dimensional representations of dynamic correlations**

331 Given a T by $\left(\frac{K^2-K}{2} + K\right)$ matrix of n^{th} -order dynamic correlations, \mathbf{Y}_n , we propose two general approaches
332 to computing a T by K low-dimensional representation of those correlations, \mathbf{X}_n . The first approach uses
333 dimensionality reduction algorithms to project \mathbf{Y}_n onto a K -dimensional space. The second approach uses
334 graph measures to characterize the relative positions of each feature ($k \in [1, \dots, K]$) in the network defined
335 by the correlation matrix at each timepoint.

336 **Dimensionality reduction-based approaches to computing \mathbf{X}_n**

337 The modern toolkit of dimensionality reduction algorithms include Principal Components Analysis²⁹ (PCA),
338 Probabilistic PCA⁵⁷ (PPCA), Exploratory Factor Analysis⁵⁸ (EFA), Independent Components Analysis^{59,60}
339 (ICA), t -Stochastic Neighbor Embedding⁶¹ (t -SNE), Uniform Manifold Approximation and Projection⁶²
340 (UMAP), non-negative matrix factorization⁶³ (NMF), Topographic Factor Analysis⁶⁴ (TFA), Hierarchical To-
341 pographic Factor analysis¹¹ (HTFA), Topographic Latent Source Analysis⁶⁵ (TLSA), dictionary learning^{66,67},
342 and deep auto-encoders⁶⁸, among others. While complete characterizations of each of these algorithms is
343 beyond the scope of the present manuscript, the general intuition driving these approaches is to compute
344 the T by K matrix, \mathbf{X} , that is closest to the original T by J matrix, \mathbf{Y} , where (typically) $K \ll J$. The different
345 approaches place different constraints on what properties \mathbf{X} must satisfy and which aspects of the data are
346 compared (and how) in order to optimize how well \mathbf{X} approximates \mathbf{Y} .

347 Applying dimensionality reduction algorithms to \mathbf{Y} yields an \mathbf{X} whose columns reflect weighted combi-
348 nations (or nonlinear transformations) of the original columns of \mathbf{Y} . This has two main consequences. First,
349 with each repeated dimensionality reduction, the resulting \mathbf{X}_n has lower and lower fidelity (with respect to
350 what the “true” \mathbf{Y}_n might have looked like without using dimensionality reduction to maintain tractability).
351 In other words, computing \mathbf{X}_n is a lossy operation. Second, whereas each column of \mathbf{Y}_n may be mapped
352 directly onto specific pairs of columns of \mathbf{X}_{n-1} , the columns of \mathbf{X}_n reflect weighted combinations and/or
353 nonlinear transformations of the columns of \mathbf{Y}_n . Many dimensionality reduction algorithms are invertible
354 (or approximately invertible). However, attempting to map a given \mathbf{X}_n back onto the original feature space
355 of \mathbf{X}_0 will usually require $O(TK^{2^n})$ space and therefore becomes intractable as n or K grow large.

356 **Graph measure approaches to computing \mathbf{X}_n**

357 The above dimensionality reduction approaches to approximating a given \mathbf{Y}_n with a lower-dimensional
358 \mathbf{X}_n preserve a (potentially recombined and transformed) mapping back to the original data in \mathbf{X}_0 . We also
359 explore graph measures that instead characterize each feature’s relative position in the broader network of

360 interactions and connections. To illustrate the distinction between the two general approaches we explore,
361 suppose a network comprises nodes A and B , along with several other nodes. If A and B exhibit uncorrelated
362 activity patterns, then by definition the functional connection (correlation) between them will be close to
363 0. However, if A and B each interact with other nodes in similar ways, we might attempt to capture those
364 similarities between A 's and B 's interactions with those other members of the network.

365 In general, graph measures take as input a matrix of interactions (e.g., using the above notation, a K
366 by K correlation matrix or binarized correlation matrix reconstituted from a single timepoint's row of \mathbf{Y}),
367 and return as output a set of K measures describing how each node (feature) sits within that correlation
368 matrix with respect to the rest of the population. Widely used measures include betweenness centrality
369 (the proportion of shortest paths between each pair of nodes in the population that involves the given
370 node in question^{69–73}); diversity and dissimilarity (characterizations of how differently connected a given
371 node is from others in the population^{74–76}); eigenvector centrality and pagerank centrality (measures of
372 how influential a given node is within the broader network^{77–80}); transfer entropy and flow coefficients
373 (a measure of how much information is flowing from a given node to other nodes in the network^{81,82});
374 k -coreness centrality (a measure of the connectivity of a node within its local subgraph^{83,84}); within-module
375 degree (a measure of how many connections a node has to its close neighbors in the network⁸⁵); participation
376 coefficient (a measure of the diversity of a node's connections to different subgraphs in the network⁸⁵); and
377 subgraph centrality (a measure of a node's participation in all of the network's subgraphs⁸⁶); among others.

378 For a given graph measure, $\eta : \mathbb{R}^{K \times K} \rightarrow \mathbb{R}^K$, we can use η to transform each row of \mathbf{Y}_n in a way that
379 characterizes the corresponding graph properties of each column. This results in a new T by K matrix,
380 \mathbf{X}_n , that reflects how the features reflected in the columns of \mathbf{X}_{n-1} participate in the network during each
381 timepoint (row).

382 Dynamic higher-order correlations

383 Because \mathbf{X}_n has the same shape as the original data \mathbf{X}_0 , approximating \mathbf{Y}_n with a lower-dimensional \mathbf{X}_n
384 enables us to estimate high-order dynamic correlations in a scalable way. Given a T by K input matrix, the
385 output of Equation 4 requires $O(TK^2)$ space to store. Repeated applications of Equation 4 (i.e., computing
386 dynamic correlations between the columns of the outputted dynamic correlation matrix) each require
387 exponentially more space; in general the n^{th} -order dynamic correlations of a T by K timeseries occupies
388 $O(TK^{2^n})$ space. However, when we approximate or summarize the output of Equation 4 with a T by K matrix
389 (as described above), it becomes feasible to compute even very high-order correlations in high-dimensional
390 data. Specifically, approximating the n^{th} -order dynamic correlations of a T by K timeseries requires only

391 $O(TK^2)$ additional space— the same as would be required to compute first-order dynamic correlations. In
 392 other words, the space required to store $n + 1$ multivariate timeseries reflecting up to n^{th} order correlations
 393 in the original data scales linearly with n using our approach (Fig. 8).

394 **Data**

395 We examined two types of data: synthetic data and human functional neuroimaging data. We constructed
 396 and leveraged the synthetic data to evaluate our general approach⁸⁷. Specifically, we tested how well
 397 Equation 4 could be used to recover known dynamic correlations using different choices of kernel (κ ; Fig. 9),
 398 for each of several synthetic datasets that exhibited different temporal properties. We also simulated higher-
 399 order correlations and tested how well Equation 4 could recover these correlations using the best kernel from
 400 the previous synthetic data analyses. We then applied our approach to a functional neuroimaging dataset
 401 to test the hypothesis that ongoing cognitive processing is reflected in high-order dynamic correlations. We
 402 used an across-participant classification test to estimate whether dynamic correlations of different orders
 403 contain information about which timepoint in a story participants were listening to.

404 **Synthetic data: simulating dynamic first-order correlations**

405 We constructed a total of 400 different multivariate timeseries, collectively reflecting a total of 4 qualitatively
 406 different patterns of dynamic first-order correlations (i.e., 100 datasets reflecting each type of dynamic pat-
 407 tern). Each timeseries comprised 50 features (dimensions) that varied over 300 timepoints. The observations
 408 at each timepoint were drawn from a zero-mean multivariate Gaussian distribution with a covariance matrix
 409 defined for each timepoint as described below. We drew the observations at each timepoint independently
 410 from the draws at all other timepoints; in other words, for each observation $s_t \sim \mathcal{N}(\mathbf{0}, \Sigma_t)$ at timepoint t ,
 411 $p(s_t) = p(s_t | s_{\setminus t})$.

Constant. We generated data with stable underlying correlations to evaluate how Equation 4 characterized correlation “dynamics” when the ground truth correlations were static. We constructed 100 multivariate timeseries whose observations were each drawn from a single (stable) Gaussian distribution. For each dataset (indexed by m), we constructed a random covariance matrix, Σ_m :

$$\Sigma_m = \mathbf{C}\mathbf{C}^\top, \text{ where} \quad (11)$$

$$\mathbf{C}(i, j) \sim \mathcal{N}(0, 1), \text{ and where} \quad (12)$$

⁴¹² $i, j \in [1, 2, \dots, 50]$. In other words, all of the observations (for each of the 300 timepoints) within each dataset
⁴¹³ were drawn from a multivariate Gaussian distribution with the same covariance matrix, and the 100 datasets
⁴¹⁴ each used a different covariance matrix.

⁴¹⁵ **Random.** We generated a second set of 100 synthetic datasets whose observations at each timepoint were
⁴¹⁶ drawn from a Gaussian distribution with a new randomly constructed (using Eqn. 11) covariance matrix.
⁴¹⁷ Because each timepoint's covariance matrix was drawn independently from the covariance matrices for all
⁴¹⁸ other timepoints, these datasets provided a test of reconstruction accuracy in the absence of any meaningful
⁴¹⁹ underlying temporal structure in the dynamic correlations underlying the data.

Ramping. We generated a third set of 100 synthetic datasets whose underlying correlations changed
gradually over time. For each dataset, we constructed two “anchor” covariance matrices using Equation 11,
 Σ_{start} and Σ_{end} . For each of the 300 timepoints in each dataset, we drew the observations from a multivariate
Gaussian distribution whose covariance matrix at each timepoint $t \in [0, \dots, 299]$ was given by

$$\Sigma_t = \left(1 - \frac{t}{299}\right)\Sigma_{\text{start}} + \frac{t}{299}\Sigma_{\text{end}}. \quad (13)$$

⁴²⁰ The gradually changing correlations underlying these datasets allow us to evaluate the recovery of dynamic
⁴²¹ correlations when each timepoint's correlation matrix is unique (as in the random datasets), but where the
⁴²² correlation dynamics are structured and exhibit first-order autocorrelations (as in the constant datasets).

⁴²³ **Event.** We generated a fourth set of 100 synthetic datasets whose underlying correlation matrices exhibited
⁴²⁴ prolonged intervals of stability, interspersed with abrupt changes. For each dataset, we used Equation 11
⁴²⁵ to generate 5 random covariance matrices. We constructed a timeseries where each set of 60 consecutive
⁴²⁶ samples was drawn from a Gaussian with the same covariance matrix. These datasets were intended to
⁴²⁷ simulate a system that exhibits periods of stability punctuated by occasional abrupt state changes.

⁴²⁸ Synthetic data: simulating dynamic high-order correlations

⁴²⁹ We developed an iterative procedure for constructing timeseries data that exhibits known dynamic high-
order correlations. The procedure builds on our approach to generating dynamic first-order correlations.
⁴³⁰ Essentially, once we generate a timeseries with known first-order correlations, we can use the known first-
⁴³¹ order correlations as a template to generate a new timeseries of second-order correlations. In turn, we can
⁴³² generate a timeseries of third-order correlations from the second-order correlations, and so on. In general,
⁴³³ we can generate order n correlations given a timeseries of order $n - 1$ correlations, for any $n > 1$. Finally,
⁴³⁴

435 given the order n timeseries, we can reverse the preceding process to generate an order $n - 1$ timeseries, an
436 order $n - 2$ order timeseries, and so on, until we obtain an order 0 timeseries of simulated data that reflects
437 the chosen high-order dynamics.

438 The central mathematical operation in our procedure is the Kronecker product (\otimes). The Kronecker
439 product of a $K \times K$ matrix, m_1 , with itself (i.e., $m_1 \otimes m_1$) produces a new $K^2 \times K^2$ matrix, m_2 whose entries
440 reflect a scaled tiling of the entries in m_1 . If these tilings (scaled copies of m_1) are indexed by row and column,
441 then the tile in the i^{th} row and j^{th} column contains the entries of m_1 , multiplied by $m_1(i, j)$. Following this
442 pattern, the Kronecker product $m_2 \otimes m_2$ yields the $K^4 \times K^4$ matrix m_3 whose tiles are scaled copies of m_2 . In
443 general, repeated applications of the Kronecker self-product may be used to generate $m_{n+1} = m_n \otimes m_n$ for
444 $n > 1$, where m_{n+1} is a $K^{2^n} \times K^{2^n}$ matrix. After generating a first-order timeseries of dynamic correlations (see
445 Synthetic data: simulating dynamic first-order correlations), we use this procedure (applied independently
446 at each timepoint) to transform it into a timeseries of n^{th} -order correlations. When m_{n+1} is generated in this
447 way, the temporal structure of the full timeseries (i.e., constant, random, ramping, event) is preserved, since
448 changes in the original first-order timeseries are also reflected in the scaled tilings of itself that comprise the
449 higher-order matrices.

450 Given a timeseries of n^{th} -order correlations, we then need to work “backwards” in order to generate the
451 order-zero timeseries. If the n^{th} -order correlation matrix at a given timepoint is m_n , then we can generate an
452 order $n - 1$ correlation matrix (for $n > 1$) by taking a draw from $\mathcal{N}(0, m_n)$ and reshaping the resulting vector
453 to have square dimensions. To force the resulting matrix to be symmetric, we remove its lower triangle, and
454 replace the lower triangle with (a reflected version of) its upper triangle. Intuitively, the re-shaped matrix
455 will look like a noisy (but symmetric) version of the template matrix, m_{n-1} . (When $n = 1$, no re-shaping
456 is needed; the resulting K -dimensional vector may be used as the observation at the given timepoint.)
457 After independently drawing each timepoint’s order $n - 1$ correlation matrix from that timepoint’s order
458 n correlation matrix, this process can be applied repeatedly until $n = 0$. This results in a K -dimensional
459 timeseries of T observations containing the specified high-order correlations at orders 1 through n . Following
460 our approach to generating synthetic data exhibiting known first-order correlations, we constructed a total
461 of 400 additional multivariate timeseries, collectively reflecting a total of 4 qualitatively different patterns of
462 dynamic correlations (i.e., 100 datasets reflecting each type of dynamic pattern: constant, random, ramping,
463 and event). Each timeseries comprised 10 zero-order features (dimensions) that varied over 300 timepoints.
464 After applying our dynamic correlation estimation procedure, this yielded a 100-dimensional timeseries of
465 first-order features that could then be used to estimate dynamic second-order correlations. (We chose to
466 use $K = 10$ zero-order features for our higher order simulations in order to put the accuracy computations
467 displayed in Figs. 2 and 3 on a roughly even footing.)

468 **Functional neuroimaging data collected during story listening**

469 We examined an fMRI dataset collected by³⁶ that the authors have made publicly available at arks.princeton.edu/ark:/88435/ds
470 The dataset comprises neuroimaging data collected as participants listened to an audio recording of a story
471 (intact condition; 36 participants), listened to temporally scrambled recordings of the same story (17 partici-
472 pants in the paragraph-scrambled condition listened to the paragraphs in a randomized order and 36 in the
473 word-scrambled condition listened to the words in a randomized order), or lay resting with their eyes open
474 in the scanner (rest condition; 36 participants). Full neuroimaging details may be found in the original paper
475 for which the data were collected³⁶. Procedures were approved by the Princeton University Committee on
476 Activities Involving Human Subjects, and by the Western Institutional Review Board (Puyallup, WA). All
477 subjects were native English speakers with normal hearing and provided written informed consent.

478 **Hierarchical topographic factor analysis (HTFA).** Following our prior related work, we used HTFA¹¹
479 to derive a compact representation of the neuroimaging data. In brief, this approach approximates the
480 timeseries of voxel activations (44,415 voxels) using a much smaller number of radial basis function (RBF)
481 nodes (in this case, 700 nodes, as determined by an optimization procedure¹¹). This provides a convenient
482 representation for examining full-brain network dynamics. All of the analyses we carried out on the
483 neuroimaging dataset were performed in this lower-dimensional space. In other words, each participant's
484 data matrix, X_0 , was a number-of-timepoints by 700 matrix of HTFA-derived factor weights (where the row
485 and column labels were matched across participants). Code for carrying out HTFA on fMRI data may be
486 found as part of the BrainIAK toolbox⁸⁸, which may be downloaded at brainiak.org.

487 **Temporal decoding**

488 We sought to identify neural patterns that reflected participants' ongoing cognitive processing of incoming
489 stimulus information. As reviewed by³⁶, one way of homing in on these stimulus-driven neural patterns is
490 to compare activity patterns across individuals (e.g., using ISFC analyses). In particular, neural patterns will
491 be similar across individuals to the extent that the neural patterns under consideration are stimulus-driven,
492 and to the extent that the corresponding cognitive representations are reflected in similar spatial patterns
493 across people⁵⁵. Following this logic, we used an across-participant temporal decoding test developed
494 by¹¹ to assess the degree to which different neural patterns reflected ongoing stimulus-driven cognitive
495 processing across people (Fig. 10). The approach entails using a subset of the data to train a classifier to
496 decode stimulus timepoints (i.e., moments in the story participants listened to) from neural patterns. We
497 use decoding (forward inference) accuracy on held-out data, from held-out participants, as a proxy for the

498 extent to which the inputted neural patterns reflected stimulus-driven cognitive processing in a similar way
499 across individuals.

500 **Forward inference and decoding accuracy**

501 We used an across-participant correlation-based classifier to decode which stimulus timepoint matched
502 each timepoint's neural pattern (Fig. 10). We first divided the participants into two groups: a template group,
503 $\mathcal{G}_{\text{template}}$ (i.e., training data), and a to-be-decoded group, $\mathcal{G}_{\text{decode}}$ (i.e., test data). We used Equation 7 to
504 compute a DISFC matrix for each group ($\bar{\mathbf{C}}_{\text{template}}$ and $\bar{\mathbf{C}}_{\text{decode}}$, respectively). We then correlated the rows of
505 $\bar{\mathbf{C}}_{\text{template}}$ and $\bar{\mathbf{C}}_{\text{decode}}$ to form a number-of-timepoints by number-of-timepoints decoding matrix, Λ . In this
506 way, the rows of Λ reflected timepoints from the template group, while the columns reflected timepoints
507 from the to-be-decoded group. We used Λ to assign temporal labels to each row $\bar{\mathbf{C}}_{\text{decode}}$ using the row of
508 $\bar{\mathbf{C}}_{\text{template}}$ with which it was most highly correlated. We then repeated this decoding procedure, but using
509 $\mathcal{G}_{\text{decode}}$ as the template group and $\mathcal{G}_{\text{template}}$ as the to-be-decoded group. Given the true timepoint labels (for
510 each group), we defined the decoding accuracy as the average proportion of correctly decoded timepoints,
511 across both groups. We defined the relative decoding accuracy as the difference between the decoding
512 accuracy and chance accuracy (i.e., $\frac{1}{T}$).

513 **Feature weighting and testing**

514 We sought to examine which types of neural features (i.e., activations, first-order dynamic correlations, and
515 higher-order dynamic correlations) were informative to the temporal decoders. Using the notation above,
516 these features correspond to $\mathbf{X}_0, \mathbf{X}_1, \mathbf{X}_2, \mathbf{X}_3$, and so on.

517 [Figure 10 about here.]

518 One challenge to fairly evaluating high-order correlations is that if the kernel used in Equation 4 is
519 wider than a single timepoint, each repeated application of the equation will result in further temporal
520 blur. Because our primary assessment metric is temporal decoding accuracy, this unfairly biases against
521 detecting meaningful signal in higher-order correlations (relative to lower-order correlations). We attempted
522 to mitigate temporal blur in estimating each \mathbf{X}_n by using a Dirac δ function kernel (which places all of its
523 mass over a single timepoint; Fig. 9b, 10a) to compute each lower-order correlation ($\mathbf{X}_1, \mathbf{X}_2, \dots, \mathbf{X}_{n-1}$). We
524 then used a new (potentially wider, as described below) kernel to compute \mathbf{X}_n from \mathbf{X}_{n-1} . In this way,
525 temporal blurring was applied only in the last step of computing \mathbf{X}_n . We note that, because each \mathbf{X}_n is a
526 low-dimensional representation of the corresponding \mathbf{Y}_n , the higher-order correlations we estimated reflect
527 true correlations in the data with lower-fidelity than estimates of lower-order correlations. Therefore, even

528 after correcting for temporal blurring, our approach is still biased against finding meaningful signal in
529 higher-order correlations.

530 After computing each $\mathbf{X}_1, \mathbf{X}_2, \dots, \mathbf{X}_{n-1}$ for each participant, we divided participants into two equally sized
531 groups (± 1 for odd numbers of participants): $\mathcal{G}_{\text{train}}$ and $\mathcal{G}_{\text{test}}$. We then further subdivided $\mathcal{G}_{\text{train}}$ into $\mathcal{G}_{\text{train}_1}$
532 and $\mathcal{G}_{\text{train}_2}$. We then computed Λ (temporal correlation) matrices for each type of neural feature, using $\mathcal{G}_{\text{train}_1}$
533 and $\mathcal{G}_{\text{train}_2}$. This resulted in $n + 1$ Λ matrices (one for the original timeseries of neural activations, and one
534 for each of n orders of dynamic correlations). Our objective was to find a set of weights for each of these
535 Λ matrices such that the weighted average of the $n + 1$ matrices yielded the highest decoding accuracy.
536 We used quasi-Newton gradient ascent⁸⁹, using decoding accuracy (for $\mathcal{G}_{\text{train}_1}$ and $\mathcal{G}_{\text{train}_2}$) as the objective
537 function to be maximized, to find an optimal set of training data-derived weights, $\phi_{0,1,\dots,n}$, where $\sum_{i=0}^n \phi_i = 1$
538 and where $\phi_i \geq 0 \forall i \in [0, 1, \dots, n]$.

539 After estimating an optimal set of weights, we computed a new set of $n + 1$ Λ matrices correlating the
540 DISFC patterns from $\mathcal{G}_{\text{train}}$ and $\mathcal{G}_{\text{test}}$ at each timepoint. We use the resulting decoding accuracy of $\mathcal{G}_{\text{test}}$
541 timepoints (using the weights in $\phi_{0,1,\dots,n}$ to average the Λ matrices) to estimate how informative the set of
542 neural features containing up to n^{th} order correlations were.

543 We used a permutation-based procedure to form stable estimates of decoding accuracy for each set of
544 neural features. In particular, we computed the decoding accuracy for each of 10 random group assignments
545 of $\mathcal{G}_{\text{train}}$ and $\mathcal{G}_{\text{test}}$. We report the mean accuracy (along with 95% confidence intervals) for each set of neural
546 features.

547 Identifying robust decoding results

548 The temporal decoding procedure we use to estimate which neural features support ongoing cognitive
549 processing is governed by several parameters. In particular, Equation 4 requires defining a kernel function,
550 which can take on different shapes and widths. For a fixed set of neural features, each of these parameters
551 can yield different decoding accuracies. Further, the best decoding accuracy for a given timepoint may be
552 reliably achieved by one set of parameters, whereas the best decoding accuracy for another timepoint might
553 be reliably achieved by a different set of parameters, and the best decoding accuracy across all timepoints
554 might be reliably achieved by still another different set of parameters. Rather than attempting to maximize
555 decoding accuracy, we sought to discover the trends in the data that were robust to classifier parameters
556 choices. Specifically, we sought to characterize how decoding accuracy varied (under different experimental
557 conditions) as a function of which neural features were considered.

558 To identify decoding results that were robust to specific classifier parameter choices, we repeated our

559 decoding analyses after substituting into Equation 4 each of a variety of kernel shapes and widths. We
560 examined Gaussian (Fig. 9c), Laplace (Fig. 9d), and Mexican Hat (Fig. 9e) kernels, each with widths of 5, 10,
561 20, and 50 samples. We then report the average decoding accuracies across all of these parameter choices.
562 This enabled us to (partially) factor out performance characteristics that were parameter-dependent, within
563 the set of parameters we examined.

564 **Reverse inference**

565 The dynamic patterns we examined comprise high-dimensional correlation patterns at each timepoint. To
566 help interpret the resulting patterns in the context of other studies, we created summary maps by computing
567 the across-timepoint average pairwise correlations at each order of analysis (first order, second order, etc.).
568 We selected the 10 strongest (absolute value) correlations at each order. Each correlation is between the
569 dynamic activity patterns (or patterns of dynamic high-order correlations) measured at two RBF nodes (see
570 Hierarchical Topographic Factor Analysis). Therefore, the 10 strongest correlations involved up to 20 RBF
571 nodes. Each RBF defines a spatial function whose activations range from 0 to 1. We constructed a map
572 of RBF components that denoted the endpoints of the 10 strongest correlations (we set each RBF to have a
573 maximum value of 1). We then carried out a meta analysis using Neurosynth³⁸ to identify the 10 terms most
574 commonly associated with the given map. This resulted in a set of 10 terms associated with the average
575 dynamic correlation patterns at each order.

576 **Data Availability**

577 The authors declare that the data supporting the findings of this study as well as the source data for
578 this paper are available at github.com/ContextLab/timecorr-paper/releases/tag/v0.4 and has been deposited
579 in the Zenodo database under accession code <https://doi.org/10.5281/zenodo.5165253>. The source data
580 underlying Figures 2–6 and Supplementary Figures S1–S9 are provided as Source Data files. Source
581 Data are provided with the manuscript. The raw fMRI data are protected and are not available due
582 to data privacy laws. The processed fMRI dataset collected by³⁶ has been made publicly available⁹¹ at
583 arks.princeton.edu/ark:/88435/dsp015d86p269k.

584 **Code Availability**

585 All of our analysis code may be downloaded from github.com/ContextLab/timecorr-paper/releases/tag/v0.4.
586 We have also published a companion Python toolbox that may be downloaded from timecorr.readthedocs.io.

587 **Acknowledgements**

588 We acknowledge discussions with Luke Chang, Vassiki Chauhan, Hany Farid, Paxton Fitzpatrick, Andrew
589 Heusser, Eshin Jolly, Aaron Lee, Qiang Liu, Matthijs van der Meer, Judith Mildner, Gina Notaro, Stephen
590 Satterthwaite, Emily Whitaker, Weizhen Xie, and Kirsten Ziman. Our work was supported in part by NSF
591 EPSCoR Award Number 1632738 to J.R.M. and by a sub-award of DARPA RAM Cooperative Agreement
592 N66001-14-2-4-032 to J.R.M. The content is solely the responsibility of the authors and does not necessarily
593 represent the official views of our supporting organizations.

594 **Author contributions**

595 Concept: J.R.M. Implementation: T.H.C., L.L.W.O., and J.R.M. Analyses: L.L.W.O. and J.R.M. Writing:
596 L.L.W.O. and J.R.M.

597 **Competing interests**

598 The authors declare no competing interests.

599 **References**

- 600 [1] Haxby, J. V. *et al.* Distributed and overlapping representations of faces and objects in ventral temporal
601 cortex. *Science* **293**, 2425–2430 (2001).
- 602 [2] Norman, K. A., Polyn, S. M., Detre, G. J. & Haxby, J. V. Beyond mind-reading: multi-voxel pattern
603 analysis of fMRI data. *Trends in Cognitive Sciences* **10**, 424–430 (2006).
- 604 [3] Tong, F. & Pratte, M. S. Decoding patterns of human brain activity. *Annual Review of Psychology* **63**,
605 483–509 (2012).
- 606 [4] Mitchell, T. M. *et al.* Predicting human brain activity associated with the meanings of nouns. *Science*
607 **320**, 1191 (2008).
- 608 [5] Kamitani, Y. & Tong, F. Decoding the visual and subjective contents of the human brain. *Nature
609 Neuroscience* **8**, 679–685 (2005).
- 610 [6] Nishimoto, S. *et al.* Reconstructing visual experience from brain activity evoked by natural movies.
611 *Current Biology* **21**, 1–6 (2011).

- 612 [7] Pereira, F. *et al.* Toward a universal decoder of linguistic meaning from brain activation. *Nature*
613 *Communications* **9**, 1–13 (2018).
- 614 [8] Huth, A. G., Nisimoto, S., Vu, A. T. & Gallant, J. L. A continuous semantic space describes the
615 representation of thousands of object and action categories across the human brain. *Neuron* **76**, 1210–
616 1224 (2012).
- 617 [9] Huth, A. G., de Heer, W. A., Griffiths, T. L., Theunissen, F. E. & Gallant, J. L. Natural speech reveals the
618 semantic maps that tile human cerebral cortex. *Nature* **532**, 453–458 (2016).
- 619 [10] Etzel, J. A., Gazzola, V. & Keysers, C. An introduction to anatomical ROI-based fMRI classification.
620 *Brain Research* **1281**, 114–125 (2009).
- 621 [11] Manning, J. R. *et al.* A probabilistic approach to discovering dynamic full-brain functional connectivity
622 patterns. *NeuroImage* **180**, 243–252 (2018).
- 623 [12] Fong, A. H. C. *et al.* Dynamic functional connectivity during task performance and rest predicts
624 individual differences in attention across studies. *NeuroImage* **188**, 14–25 (2019).
- 625 [13] Grossberg, S. Nonlinear neural networks: principles, mechanisms, and architectures. *Neural Networks*
626 **1**, 17–61 (1988).
- 627 [14] Friston, K. J. The labile brain. I. neuronal transients and nonlinear coupling. *Philosophical Transactions
628 of the Royal Society of London* **355B**, 215–236 (2000).
- 629 [15] Sporns, O. & Honey, C. J. Small worlds inside big brains. *Proceedings of the National Academy of Sciences,
630 USA* **103**, 19219–19220 (2006).
- 631 [16] Bassett, D., Meyer-Lindenberg, A., Achard, S., Duke, T. & Bullmore, E. Adaptive reconfiguration of
632 fractal small-world human brain functional networks. *Proceedings of the National Academy of Sciences,
633 USA* **103**, 19518–19523 (2006).
- 634 [17] Turk-Browne, N. B. Functional interactions as big data in the human brain. *Science* **342**, 580–584 (2013).
- 635 [18] Demertzi, A. *et al.* Human consciousness is supported by dynamic complex patterns of brain signal
636 coordination. *Science Advances* **5**, eaat7603 (2019).
- 637 [19] Solomon, S. H., Medaglia, J. D. & Thompson-Schill, S. L. Implementing a concept network model.
638 *Behavior Research Methods* **51**, 1717–1736 (2019).

- 639 [20] Lurie, D. *et al.* On the nature of time-varying functional connectivity in resting fMRI. *PsyArXiv*
640 doi.org/10.31234/osf.io/xtzre (2018).
- 641 [21] Preti, M. G., Bolton, T. A. W. & Van De Ville, D. The dynamic functional connectome: state-of-the-art
642 and perspectives. *NeuroImage* **160**, 41–54 (2017).
- 643 [22] Zou, Y., Donner, R. V., Marwan, N., Donges, J. F. & Kurths, J. Complex network approaches to nonlinear
644 time series analysis. *Physics Reports* **787**, 1–97 (2019).
- 645 [23] Mack, M. L., Preston, A. R. & Love, B. C. Medial prefrontal cortex compresses concept representations
646 through learning. *bioRxiv* doi.org/10.1101/178145 (2017).
- 647 [24] Bressler, S. L. & Kelso, J. A. S. Cortical coordination dynamics and cognition. *Trends in Cognitive Sciences*
648 **5**, 26–36 (2001).
- 649 [25] McIntosh, A. R. Towards a network theory of cognition. *Neural Networks* **13**, 861–870 (2000).
- 650 [26] Reimann, M. W. *et al.* Cliques of neurons bound into cavities provide a missing link between structure
651 and function. *Frontiers in Computational Neuroscience* **11**, 1–16 (2017).
- 652 [27] Beaty, R. E., Benedek, M., Silvia, P. J. & Schacter, D. L. Creative cognition and brain network dynamics.
653 *Trends in Cognitive Sciences* **20**, 87–95 (2016).
- 654 [28] Bullmore, E. & Sporns, O. Complex brain networks: graph theoretical analysis of structural and
655 functional systems. *Nature Reviews Neuroscience* **10**, 186–198 (2009).
- 656 [29] Pearson, K. On lines and planes of closest fit to systems of points in space. *The London, Edinburgh, and*
657 *Dublin Philosophical Magazine and Journal of Science* **2**, 559–572 (1901).
- 658 [30] McIntosh, A. R. & Jirsa, V. K. The hidden repertoire of brain dynamics and dysfunction. *Network*
659 *Neuroscience* doi.org/10.1162/netn_a_00107 (2019).
- 660 [31] Toker, D. & Sommer, F. T. Information integration in large brain networks. *PLoS Computational Biology*
661 **15**, e1006807 (2019).
- 662 [32] Gonzalez-Castillo, J. *et al.* Imaging the spontaneous flow of thought: distinct periods of cognition
663 contribute to dynamic functional connectivity during rest. *NeuroImage* **202** (2019).
- 664 [33] Landau, E. Zur relativen Wertbemessung der Turnierresultate. *Deutsches Wochenschach* **11**, 366–369
665 (1895).

- 666 [34] Betzel, R. F., Byrge, L., Esfahlani, F. Z. & Kennedy, D. P. Temporal fluctuations in the brain's modular
667 architecture during movie-watching. *bioRxiv* doi.org/10.1101/750919 (2019).
- 668 [35] Sizemore, A. E. *et al.* Cliques and cavities in the human connectome. *Journal of Computational Neuroscience*
669 **44**, 115–145 (2018).
- 670 [36] Simony, E., Honey, C. J., Chen, J. & Hasson, U. Dynamic reconfiguration of the default mode network
671 during narrative comprehension. *Nature Communications* **7**, 1–13 (2016).
- 672 [37] Hasson, U., Yang, E., Vallines, I., Heeger, D. J. & Rubin, N. A hierarchy of temporal receptive windows
673 in human cortex. *The Journal of Neuroscience* **28**, 2539–2550 (2008).
- 674 [38] Rubin, T. N. *et al.* Decoding brain activity using a large-scale probabilistic functional-anatomical atlas
675 of human cognition. *PLoS Computational Biology* **13**, e1005649 (2017).
- 676 [39] Park, H.-J., Friston, K. J., Pae, C., Park, B. & Razi, A. Dynamic effective connectivity in resting state
677 fMRI. *NeuroImage* **180**, 594–608 (2018).
- 678 [40] Roy, D. S. *et al.* Brain-wide mapping of contextual fear memory engram ensembles supports the
679 dispersed engram complex hypothesis. *bioRxiv* doi.org/10.1101/668483 (2019).
- 680 [41] Liégeois, R. *et al.* Resting brain dynamics at different timescales capture distinct aspects of human
681 behavior. *Nature Communications* **10**, 1–9 (2019).
- 682 [42] Chang, C. & Glover, G. H. Time-frequency dynamics of resting-state brain connectivity measured with
683 fMRI. *NeuroImage* **50**, 81–98 (2010).
- 684 [43] Zheng, M., Allard, A., Hagmann, P. & Serrano, M. . . A. Geometric renormalization unravels self-
685 similarity of the multiscale human connectome. *arXiv* 1904.11793 (2019).
- 686 [44] Baldassano, C. *et al.* Discovering event structure in continuous narrative perception and memory.
687 *Neuron* **95**, 709–721 (2017).
- 688 [45] Hasson, U., Chen, J. & Honey, C. J. Hierarchical process memory: memory as an integral component
689 of information processing. *Trends in Cognitive Sciences* **19**, 304–315 (2015).
- 690 [46] Honey, C. J. *et al.* Slow cortical dynamics and the accumulation of information over long timescales.
691 *Neuron* **76**, 423–434 (2012).
- 692 [47] Lerner, Y., Honey, C. J., Silbert, L. J. & Hasson, U. Topographic mapping of a hierarchy of temporal
693 receptive windows using a narrated story. *The Journal of Neuroscience* **31**, 2906–2915 (2011).

- 694 [48] Lerner, Y., Honey, C. J., Katkov, M. & Hasson, U. Temporal scaling of neural responses to compressed
695 and dilated natural speech. *Journal of Neurophysiology* **111**, 2433–2444 (2014).
- 696 [49] Chien, H.-Y. S. & Honey, C. J. Constructing and forgetting temporal context in the human cerebral
697 cortex. *bioRxiv* **doi.org/10.1101/761593** (2019).
- 698 [50] Lee, C. S., Aly, M. & Baldassano, C. Anticipation of temporally structured events in the brain. *bioRxiv*
699 **10.1101/2020.10.14.338145** (2020).
- 700 [51] Fallon, J., Ward, P. G. D., Parkes, L. & Oldham, S. Timescales of spontaneous fMRI fluctuations relate
701 to structural connectivity in the brain. *Network Neuroscience* **4**, 788–806 (2020).
- 702 [52] Shappell, H., Caffo, B. S., Pekar, J. J. & Lindquist, M. A. Improved state change estimation in dynamic
703 functional connectivity using hidden semi-Markov models. *NeuroImage* **191**, 243–257 (2019).
- 704 [53] Vidaurre, D. *et al.* Discovering dynamic brain networks from big data in rest and task. *NeuroImage* **180**,
705 646–656 (2018).
- 706 [54] Allen, E. A. *et al.* Tracking whole-brain connectivity dynamics in the resting state. *Cerebral Cortex* **24**,
707 663–676 (2012).
- 708 [55] Simony, E. & Chang, C. Analysis of stimulus-induced brain dynamics during naturalistic paradigms.
709 *NeuroImage* **216**, 116461 (2020).
- 710 [56] Zar, J. H. *Biostatistical analysis* (Prentice-Hall, 2010).
- 711 [57] Tipping, M. E. & Bishop, C. M. Probabilistic principal component analysis. *Journal of Royal Statistical
712 Society, Series B* **61**, 611–622 (1999).
- 713 [58] Spearman, C. General intelligence, objectively determined and measured. *American Journal of Psychology*
714 **15**, 201–292 (1904).
- 715 [59] Jutten, C. & Herault, J. Blind separation of sources, part I: an adaptive algorithm based on neuromimetic
716 architecture. *Signal Processing* **24**, 1–10 (1991).
- 717 [60] Comon, P., Jutten, C. & Herault, J. Blind separation of sources, part II: problems statement. *Signal
718 Processing* **24**, 11–20 (1991).
- 719 [61] van der Maaten, L. J. P. & Hinton, G. E. Visualizing high-dimensional data using t-SNE. *Journal of
720 Machine Learning Research* **9**, 2579–2605 (2008).

- 721 [62] McInnes, L., Healy, J. & Melville, J. UMAP: uniform manifold approximation and projection for
722 dimension reduction. *arXiv* **1802** (2018).
- 723 [63] Lee, D. D. & Seung, H. S. Learning the parts of objects by non-negative matrix factorization. *Nature*
724 **401**, 788–791 (1999).
- 725 [64] Manning, J. R., Ranganath, R., Norman, K. A. & Blei, D. M. Topographic factor analysis: a Bayesian
726 model for inferring brain networks from neural data. *PLoS One* **9**, e94914 (2014).
- 727 [65] Gershman, S. J., Blei, D. M., Pereira, F. & Norman, K. A. A topographic latent source model for fMRI
728 data. *NeuroImage* **57**, 89–100 (2011).
- 729 [66] Mairal, J. B., Bach, F., Ponce, J. & Sapiro, G. Online dictionary learning for sparse coding. *Proceedings*
730 *of the International Conference on Machine Learning* 689–696 (2009).
- 731 [67] Mairal, J., Ponce, J., Sapiro, G., Zisserman, A. & Bach, F. R. Supervised dictionary learning. *Advances*
732 *in Neural Information Processing Systems* 1033–1040 (2009).
- 733 [68] Hinton, G. E. & Salakhutdinov, R. R. Reducing the dimensionality of data with neural networks. *Science*
734 **313**, 504–507 (2006).
- 735 [69] Newman, M. E. J. A measure of betweenness centrality based on random walks. *Social Networks* **27**,
736 39–54 (2005).
- 737 [70] Opsahl, T., Agneessens, F. & Skvoretz, J. Node centrality in weighted networks: generalizing degree
738 and shortest paths. *Social Networks* **32**, 245–251 (2010).
- 739 [71] Barthélemy, M. Betweenness centrality in large complex networks. *European Physical Journal B* **38**,
740 163–168 (2004).
- 741 [72] Geisberger, R., Sanders, P. & Schultes, D. Better approximation of betweenness centrality. *Proceedings*
742 *of the Meeting on Algorithm Engineering and Experiments* 90–100 (2008).
- 743 [73] Freeman, L. C. A set of measures of centrality based on betweenness. *Sociometry* **40**, 35–41 (1977).
- 744 [74] Rao, C. R. Diversity and dissimilarity coefficients: a unified approach. *Theoretical Population Biology* **21**,
745 24–43 (1982).
- 746 [75] Lin, J. Divergence measures based on the Shannon entropy. *IEEE Transactions on Information Theory* **37**,
747 145–151 (2009).

- 748 [76] Ricotta, C. & Szeidl, L. Towards a unifying approach to diversity measures: bridging the gap between
749 the Shannon entropy and Rao's quadratic index. *Theoretical Population Biology* **70**, 237–243 (2006).
- 750 [77] Newman, M. E. J. The mathematics of networks. *The New Palgrave Encyclopedia of Economics* **2**, 1–12
751 (2008).
- 752 [78] Bonacich, P. Some unique properties of eigenvector centrality. *Social Networks* **29**, 555–564 (2007).
- 753 [79] Lohmann, G. *et al.* Eigenvector centrality mapping for analyzing connectivity patterns in fMRI data of
754 the human brain. *PLoS One* **5**, e10232 (2010).
- 755 [80] Halu, A., Mondragón, R. J., Panzarasa, P. & Bianconi, G. Multiplex PageRank. *PLoS One* **8**, e78293
756 (2013).
- 757 [81] Honey, C. J., Kötter, R., Breakspear, M. & Sporns, O. Network structure of cerebral cortex shapes
758 functional connectivity on multiple time scales. *Proceedings of the National Academy of Sciences, USA* **104**,
759 10240–10245 (2007).
- 760 [82] Schreiber, T. Measuring information transfer. *Physical Review Letters* **85**, 461–464 (2000).
- 761 [83] Alvarez-Hamelin, I., Dall'Asta, L., Barrat, A. & Vespignani, A. *k*-corr decomposition: a tool for the
762 visualiztion of large scale networks. *arXiv cs/0504107v2* (2005).
- 763 [84] Christakis, N. A. & Fowler, J. H. Social network sensors for early detection of contagious outbreaks.
764 *PLoS One* **5**, e12948 (2010).
- 765 [85] Rubinov, M. & Sporns, O. Complex network measures of brain connectivity: uses and interpretations.
766 *NeuroImage* **52**, 1059–1069 (2010).
- 767 [86] Estrada, E. & Rodríguez-Velázquez, J. A. Subgraph centrality in complex networks. *Physical Review E*
768 **71**, 056103 (2005).
- 769 [87] Thompson, W. H., Richter, C. G., Plavén-Sigray, P. & Fransson, P. Simulations to benchmark time-
770 varying connectivity methods for fMRI. *PLoS Computational Biology* **14**, e1006196 (2018).
- 771 [88] Capota, M. *et al.* Brain imaging analysis kit (2017).
- 772 [89] Nocedal, J. & Wright, S. J. *Numerical optimization* (Springer, New York, NY, 2006).
- 773 [90] Combrisson, E. *et al.* Visbrain: a multi-purpose GPU-accelerated open-source suite for multimodal
774 brain data visualization. *Frontiers in Neuroinformatics* **13**, 1–14 (2019).

775 [91] Simony, E., Honey, C. J., Chen, J. & Hasson, U. Dynamic reconfiguration of the default mode network
776 during narrative comprehension. *DataSpace* <http://arks.princeton.edu/ark:/88435/dsp015d86p269k>
777 (2016).

778 **Figures**

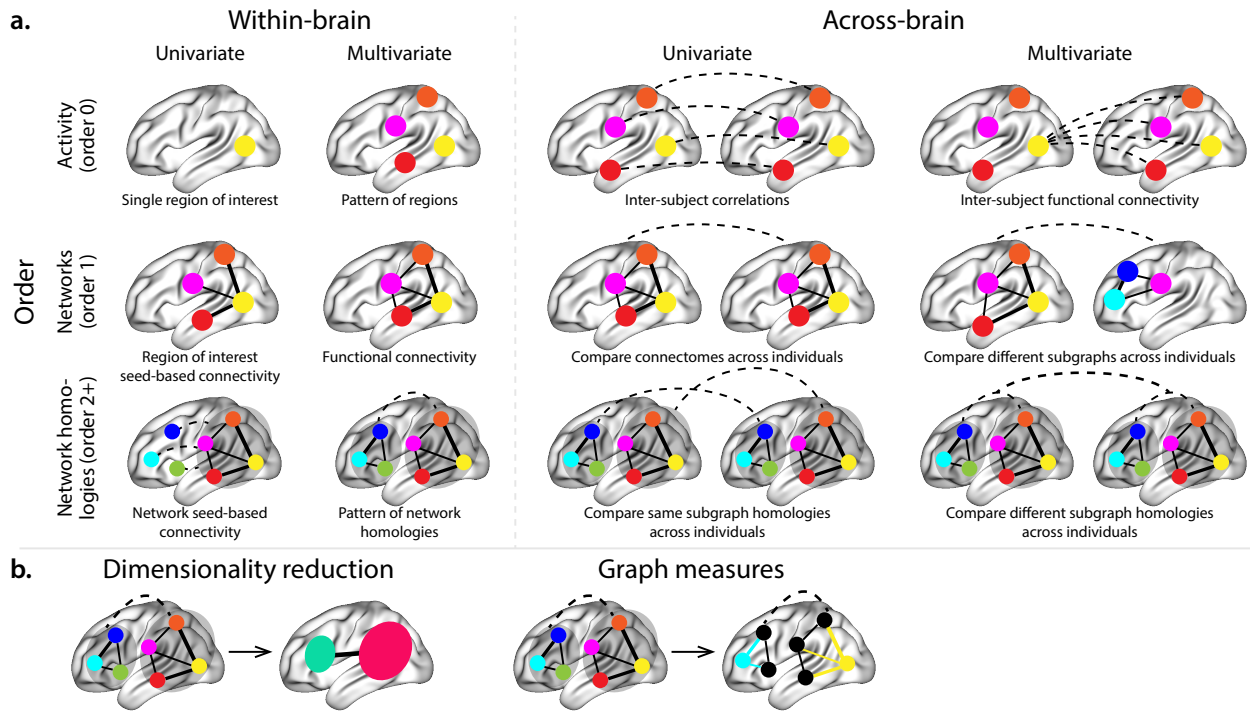


Figure 1: Neural patterns. a. A space of neural features. Within-brain analyses are carried out within a single brain, whereas across-brain analyses compare neural patterns across two or more individuals' brains. Univariate analyses characterize the activities of individual units (e.g., nodes, small networks, hierarchies of networks, etc.), whereas multivariate analyses characterize the patterns of activity across units. Order 0 patterns involve individual nodes; order 1 patterns involve node-node interactions; order 2 (and higher) patterns relate to interactions between homologous networks. Each of these patterns may be static (e.g., averaging over time) or dynamic. **b. Summarizing neural patterns.** To efficiently compute with complex neural patterns, it can be useful to characterize the patterns using summary measures. Dimensionality reduction algorithms project the patterns onto lower-dimensional spaces whose dimensions reflect weighted combinations or non-linear transformations of the dimensions in the original space. Graph measures characterize each unit's participation in its associated network.

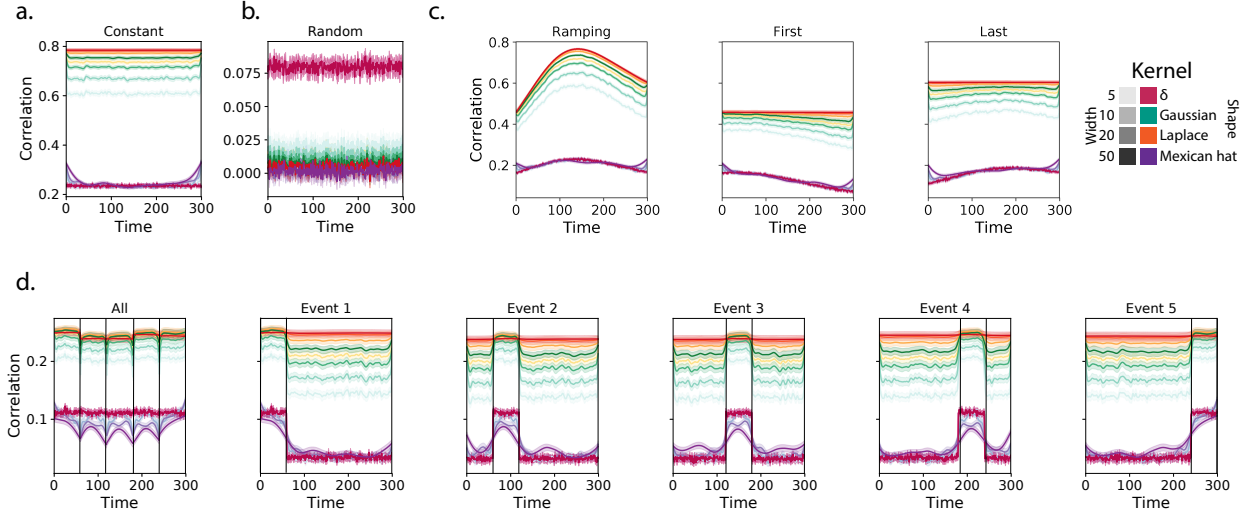


Figure 2: Recovering known dynamic first-order correlations from synthetic data. Each panel displays the average correlations between the vectorized upper triangles of the recovered correlation matrix at each timepoint and either the true underlying correlation at each timepoint or a reference correlation matrix. (The averages are taken across 100 different randomly generated synthetic datasets of each given category, each with $K = 50$ features and $T = 300$ timepoints.) Error ribbons denote 95% confidence intervals of the mean (taken across datasets). Different colors denote different kernel shapes, and the shading within each color family denotes the kernel width parameter. For a complete description of each synthetic dataset, see Synthetic data: simulating dynamic first-order correlations. **a. Constant correlations.** These datasets have a stable (unchanging) underlying correlation matrix. **b. Random correlations.** These datasets are generated using a new independently drawn correlation matrix at each new timepoint. **c. Ramping correlations.** These datasets are generated by smoothly varying the underlying correlations between the randomly drawn correlation matrices at the first and last timepoints. The left panel displays the correlations between the recovered dynamic correlations and the underlying ground truth correlations. The middle panel compares the recovered correlations with the first timepoint's correlation matrix. The right panel compares the recovered correlations with the last timepoint's correlation matrix. **d. Event-based correlations.** These datasets are each generated using five randomly drawn correlation matrices that each remain stable for a fifth of the total timecourse. The left panel displays the correlations between the recovered dynamic correlations and the underlying ground truth correlations. The right panels compare the recovered correlations with the correlation matrices unique to each event. The vertical lines denote event boundaries. Source data are provided as a Source Data file.

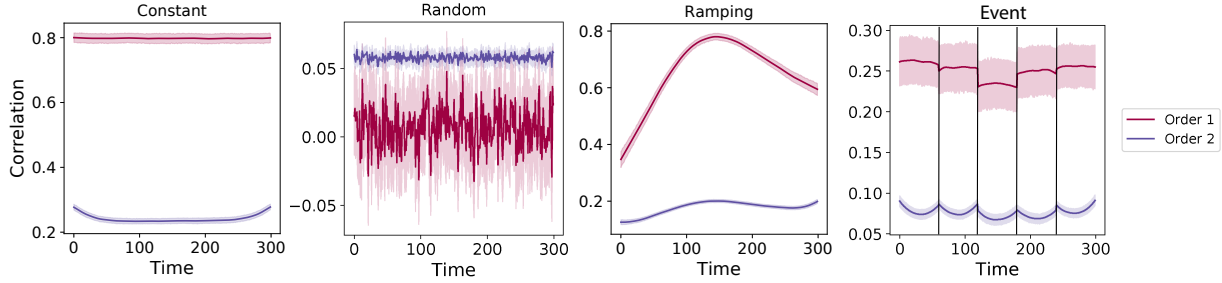


Figure 3: Recovery of simulated first-order and second-order dynamic correlations. Each panel displays the average correlations between the vectorized upper triangles of the recovered first-order and second-order correlation matrices and the true (simulated) first-order and second order correlation matrices at each timepoint and for each synthetic dataset. (The averages are taken across 100 different randomly generated synthetic datasets of each given category, each with $K = 10$ features and $T = 300$ timepoints.) Error ribbons denote 95% confidence intervals of the mean (taken across datasets). For a complete description of each synthetic dataset, see Synthetic data: simulating dynamic higher-order correlations. All estimates represented in this figure were computed using a Laplace kernel (width = 20). **Constant.** These datasets have stable (unchanging) underlying second-order correlation matrices. **Random.** These datasets are generated using a new independently drawn second-order correlation matrix at each timepoint. **Ramping.** These datasets are generated by smoothly varying the underlying second-order correlations between the randomly drawn correlation matrices at the first and last timepoints. **Event.** These datasets are each generated using five randomly drawn second-order correlation matrices that each remain stable for a fifth of the total timecourse. The vertical lines denote event boundaries. Note that the “dips” and “ramps” at the boundaries of sharp transitions (e.g., the beginning and ends of the “constant” and “ramping” datasets, and at the event boundaries of the “event” datasets) are finite-sample effects that reflect the reduced numbers of samples that may be used to accurately estimate correlations at sharp boundaries. Source data are provided as a Source Data file.

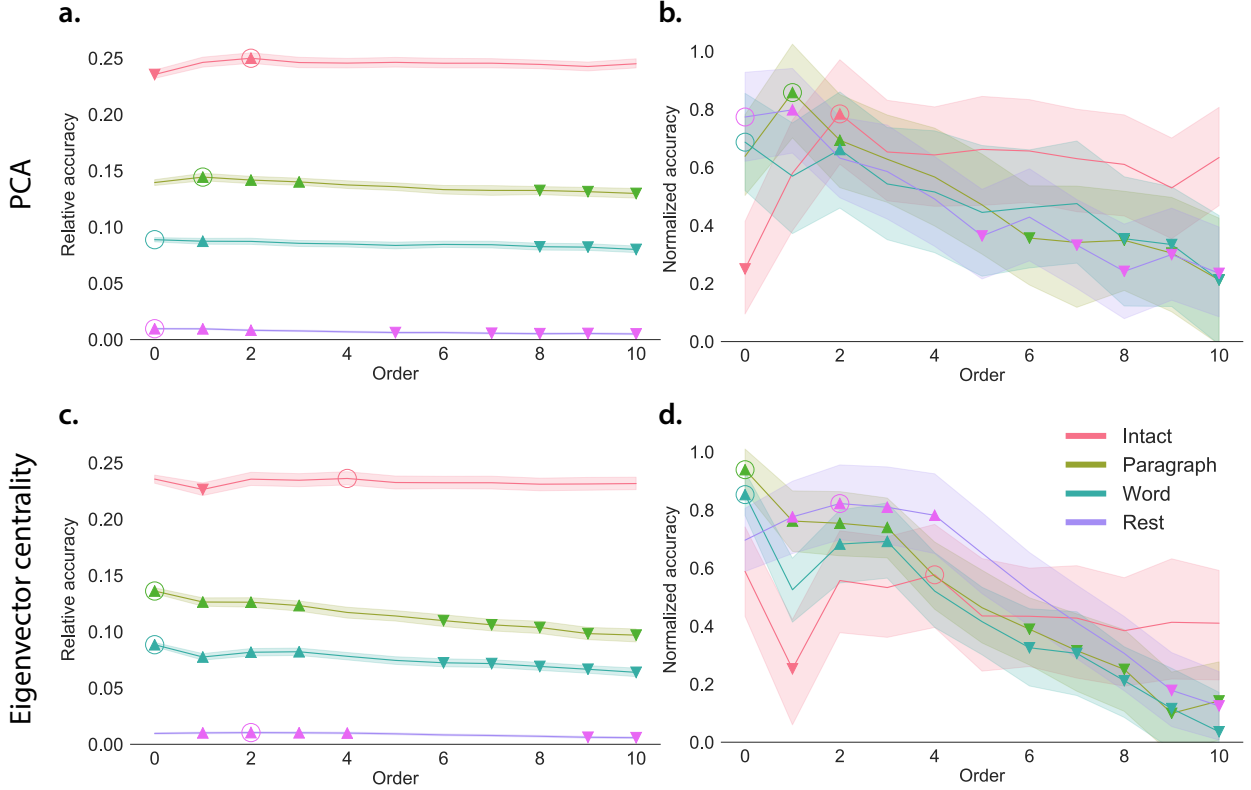


Figure 4: Across-participant timepoint decoding accuracy varies with correlation order and cognitive engagement.

a. Decoding accuracy as a function of order: PCA. “Order” (x-axis) refers to the maximum order of dynamic correlations that were available to the classifiers (see Feature weighting and testing). The reported across-participant decoding accuracies are averaged over all kernel shapes and widths (see Identifying robust decoding results). The y-values are displayed relative to chance accuracy (intact: $\frac{1}{300}$; paragraph: $\frac{1}{272}$; word: $\frac{1}{300}$; rest: $\frac{1}{400}$; these chance accuracies were subtracted from the observed accuracies to obtain the relative accuracies reported on the y-axis). The error ribbons denote 95% confidence intervals of the means across cross-validation folds (i.e., random assignments of participants to the training and test sets). The colors denote the experimental condition. Arrows denote sets of features that yielded reliably higher (upward facing) or lower (downward facing) decoding accuracy than the mean of all other features (via a two-tailed *t*-test, thresholded at $p < 0.05$). Figure 5 displays additional comparisons between the decoding accuracies achieved using different sets of neural features. The circled values represent the maximum decoding accuracy within each experimental condition.

b. Normalized timepoint decoding accuracy as a function of order: PCA. This panel displays the same results as Panel a, but here each curve has been normalized to have a maximum value of 1 and a minimum value of 0 (including the upper and lower bounds of the respective 95% confidence intervals of the mean).

c. Timepoint decoding accuracy as a function of order: eigenvector centrality. This panel is in the same format as Panel a, but here eigenvector centrality has been used to project the high-dimensional patterns of dynamic correlations onto a lower-dimensional space.

d. Normalized timepoint decoding accuracy as a function of order: eigenvector centrality. This panel is in the same format as Panel b, but here eigenvector centrality has been used to project the high-dimensional patterns of dynamic correlations onto a lower-dimensional space. See Figures S1 and S2 for decoding results broken down by kernel shape and width, respectively. Source data are provided as a Source Data file.

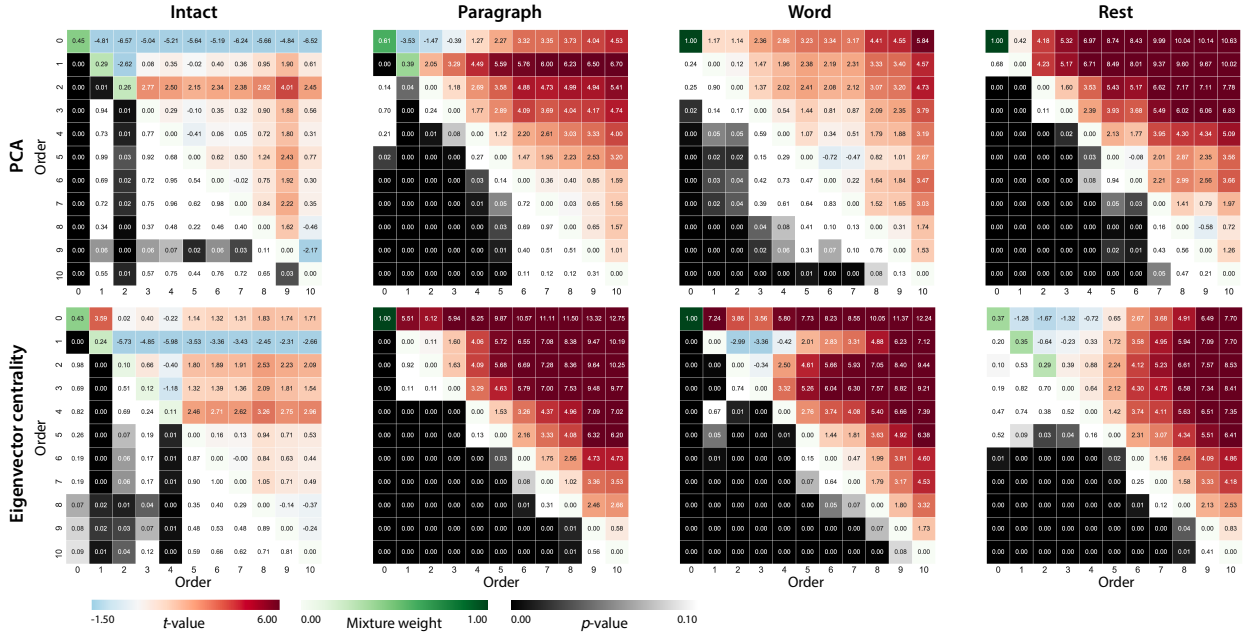


Figure 5: Statistical summary of decoding accuracies for different neural features. Each column of matrices displays decoding results for one experimental condition (intact, paragraph, word, and rest). We considered dynamic activity patterns (order 0) and dynamic correlations at different orders (order > 0). We used two-tailed t -tests to compare the distributions of decoding accuracies obtained using each pair of features. The distributions for each feature reflect the set of average decoding accuracies (across all kernel parameters), obtained for each random assignment of training and test groups. In the upper triangles of each matrix, warmer colors (positive t -values) indicate that the neural feature indicated in the given row yielded higher accuracy than the feature indicated in the given column. Cooler colors (negative t -values) indicate that the feature in the given row yielded lower decoding accuracy than the feature in the given column. The lower triangles of each map denote the corresponding p -values for the t -tests. The diagonal entries display the relative average optimized weight given to each type of feature in a decoder that included all feature types (see Feature weighting and testing). Source data are provided as a Source Data file.

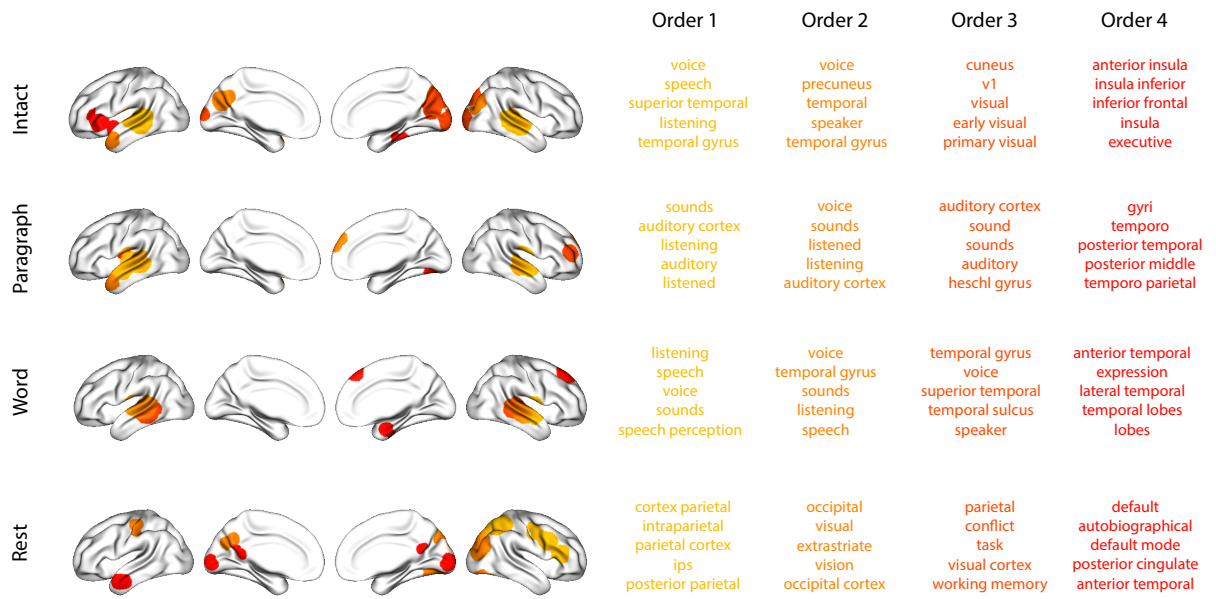


Figure 6: Top terms associated with the most strongly correlated nodes at each order. Each color corresponds to one order of inter-subject functional correlations. To calculate the dynamic correlations, eigenvector centrality has been used to project the high-dimensional patterns of dynamic correlations onto a lower-dimensional space at each previous order, which allows us to map the brain regions at each order by retaining the features of the original space. The inflated brain plots display the locations of the endpoints of the 10 strongest (absolute value) correlations at each order, thresholded at 0.999, and projected onto the cortical surface⁹⁰. The lists of terms on the right display the top five Neurosynth terms³⁸ decoded from the corresponding brain maps for each order. Each row displays data from a different experimental condition. Additional maps and their corresponding Neurosynth terms may be found in the Supplementary materials (intact: Fig. S5; paragraph: Fig. S6; word: Fig. S7; rest: Fig. S8). Source data are provided as a Source Data file.

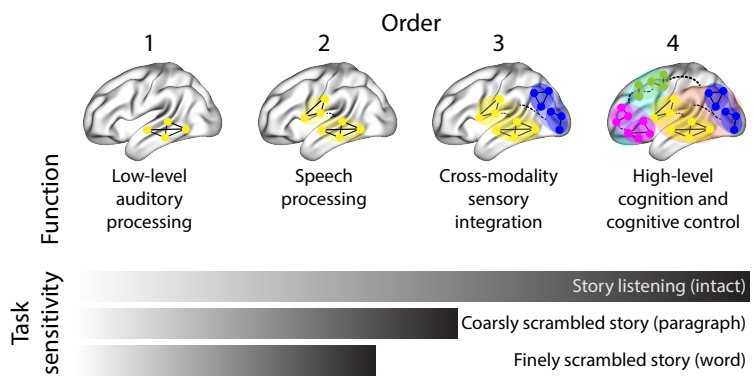


Figure 7: Proposed high-order network dynamics underlying high-level cognition during story listening. Schematic depicts higher orders of network interactions supporting higher-level aspects of cognitive processing. When tasks evoke richer, deeper, and/or higher-level processing, this is reflected in higher-order network interactions.

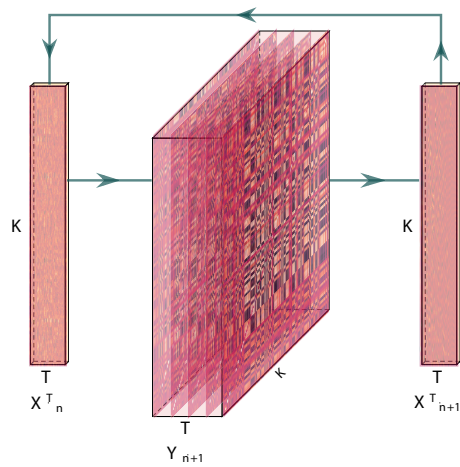


Figure 8: Estimating dynamic high-order correlations. Given a T by K matrix of multivariate timeseries data, \mathbf{X}_n (where $n \in \mathbb{N}, n \geq 0$), we use Equation 4 to compute a timeseries of K by K correlation matrices, \mathbf{Y}_{n+1} . We then approximate \mathbf{Y}_{n+1} with the T by K matrix \mathbf{X}_{n+1} . This process may be repeated to scalably estimate iteratively higher-order correlations in the data. Note that the transposes of \mathbf{X}_n and \mathbf{X}_{n+1} are displayed in the figure for compactness.

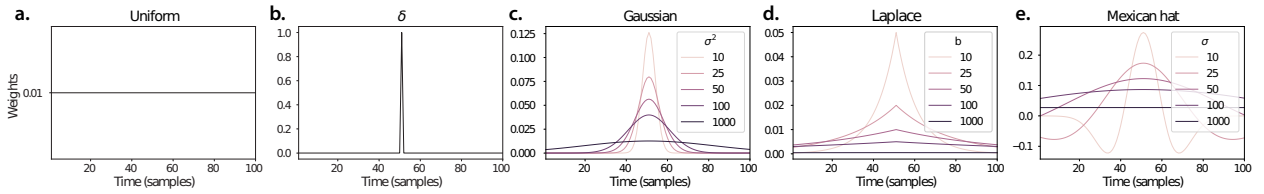


Figure 9: Examples of kernel functions. Each panel displays per-timepoint weights for a kernel centered at $t = 50$, evaluated at 100 timepoints ($\tau \in [1, \dots, 100]$). **a. Uniform kernel.** The weights are timepoint-invariant; observations at all timepoints are weighted equally, and do not change as a function of τ . This is a special case kernel function that reduces dynamic correlations to static correlations. **b. Dirac δ kernel.** Only the observation at timepoint t is given a non-zero weight (of 1). **c. Gaussian kernels.** Each kernel's weights fall off in time according to a Gaussian probability density function centered on time t . Weights derived using several different example width parameters (σ^2) are displayed. **d. Laplace kernels.** Each kernel's weights fall off in time according to a Laplace probability density function centered on time t . Weights derived using several different example width parameters (b) are displayed. **e. Mexican hat (Ricker wavelet) kernels.** Each kernel's weights fall off in time according to a Ricker wavelet centered on time t . This function highlights the contrasts between local versus surrounding activity patterns in estimating dynamic correlations. Weights derived using several different example width parameters (σ) are displayed.

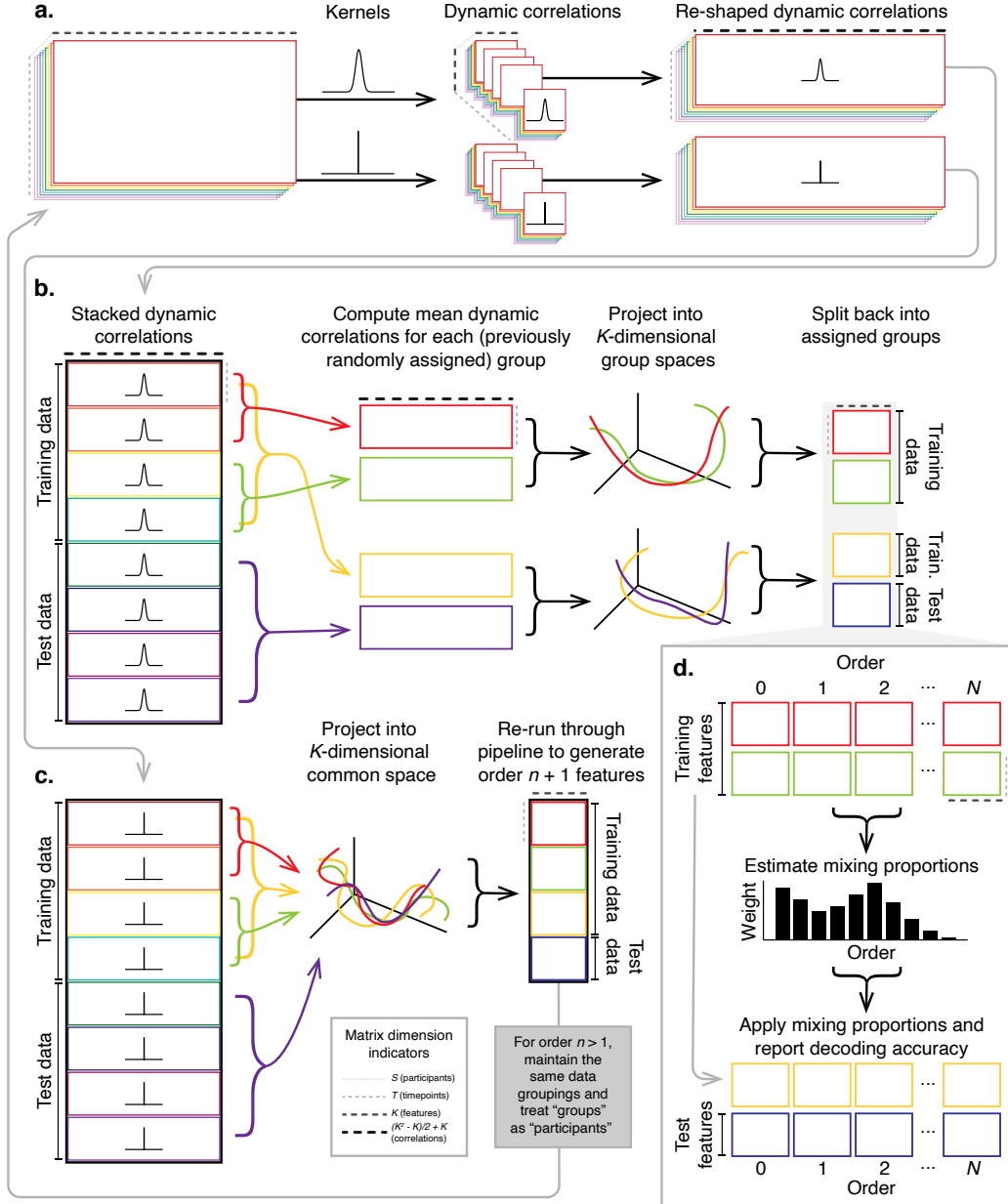


Figure 10: Decoding analysis pipeline. **a. Computing dynamic correlations from timeseries data.** Given a timeseries of observations as a $T \times K$ matrix (or a set of S such matrices), we use Equation 4 to compute each participant's DISFC (relative to other participants in the training or test sub-group, as appropriate). We repeat this process twice—once using the analysis kernel (shown here as a Gaussian in the upper row of the panel), and once using a δ function kernel (lower row of the panel). **b. Projecting dynamic correlations into a lower-dimensional space.** We project the training and test data into K -dimensional spaces to create compact representations of dynamic correlations at the given order (estimated using the analysis kernel). **c. Kernel trick.** We project the dynamic correlations computed using a δ function kernel into a common K -dimensional space. These low-dimensional embeddings are fed back through the analysis pipeline in order to compute features at the next-highest order. **d. Decoding analysis.** We split the training data into two equal groups, and optimize the feature weights (i.e., dynamic correlations at each order) to maximize decoding accuracy. We then apply the trained classifier to the (held-out) test data.